



**HAL**  
open science

# A measles-vectored vaccine candidate expressing prefusion-stabilized SARS-CoV-2 spike protein brought to phase I/II clinical trials: candidate selection in a preclinical murine model

Jérémy Brunet, Zaineb Choucha, Marion Gransagne, Houda Tabbal, Min-Wen Ku, Julian Buchrieser, Priyanka Fernandes, Damien Batalie, Jodie Lopez, Laurence Ma, et al.

## ► To cite this version:

Jérémy Brunet, Zaineb Choucha, Marion Gransagne, Houda Tabbal, Min-Wen Ku, et al.. A measles-vectored vaccine candidate expressing prefusion-stabilized SARS-CoV-2 spike protein brought to phase I/II clinical trials: candidate selection in a preclinical murine model. *Journal of Virology*, 2024, 98 (5), pp.e01693-23. 10.1128/jvi.01693-23 . pasteur-04601117

**HAL Id: pasteur-04601117**

**<https://pasteur.hal.science/pasteur-04601117v1>**

Submitted on 4 Jun 2024

**HAL** is a multi-disciplinary open access archive for the deposit and dissemination of scientific research documents, whether they are published or not. The documents may come from teaching and research institutions in France or abroad, or from public or private research centers.

L'archive ouverte pluridisciplinaire **HAL**, est destinée au dépôt et à la diffusion de documents scientifiques de niveau recherche, publiés ou non, émanant des établissements d'enseignement et de recherche français ou étrangers, des laboratoires publics ou privés.

Copyright

# A measles-vectored vaccine candidate expressing prefusion-stabilized SARS-CoV-2 spike protein brought to phase I/II clinical trials: candidate selection in a preclinical murine model

Jérémy Brunet,<sup>1</sup> Zaineb Choucha,<sup>1</sup> Marion Gransagne,<sup>1</sup> Houda Tabbal,<sup>2</sup> Min-Wen Ku,<sup>3</sup> Julian Buchrieser,<sup>4</sup> Priyanka Fernandes,<sup>5</sup> Damien Batalie,<sup>2</sup> Jodie Lopez,<sup>3</sup> Laurence Ma,<sup>6</sup> Evelyne Dufour,<sup>7</sup> Emeline Simon,<sup>2</sup> David Hardy,<sup>8</sup> Stéphane Petres,<sup>7</sup> Françoise Guinet,<sup>9</sup> Helene Strick-Marchand,<sup>5</sup> Marc Monot,<sup>6</sup> Pierre Charneau,<sup>3</sup> Laleh Majlessi,<sup>3</sup> W. Paul Duprex,<sup>10</sup> Christiane Gerke,<sup>11</sup> Annette Martin,<sup>2</sup> Nicolas Escriou<sup>1</sup>

**AUTHOR AFFILIATIONS** See affiliation list on p. 33.

**ABSTRACT** In the early COVID-19 pandemic with urgent need for countermeasures, we aimed at developing a replicating viral vaccine using the highly efficacious measles vaccine as vector, a promising technology with prior clinical proof of concept. Building on our successful pre-clinical development of a measles virus (MV)-based vaccine candidate against the related SARS-CoV, we evaluated several recombinant MV expressing codon-optimized SARS-CoV-2 spike glycoprotein. Candidate V591 expressing a prefusion-stabilized spike through introduction of two proline residues in HR1 hinge loop, together with deleted S1/S2 furin cleavage site and additional inactivation of the endoplasmic reticulum retrieval signal, was the most potent in eliciting neutralizing antibodies in mice. After single immunization, V591 induced similar neutralization titers as observed in sera of convalescent patients. The cellular immune response was confirmed to be Th1 skewed. V591 conferred long-lasting protection against SARS-CoV-2 challenge in a murine model with marked decrease in viral RNA load, absence of detectable infectious virus loads, and reduced lesions in the lungs. V591 was furthermore efficacious in an established non-human primate model of disease (see companion article [S. Nambulli, N. Escriou, L. J. Rennick, M. J. Demers, N. L. Tilston-Lunel et al., *J Virol* 98:e01762-23, 2024, <https://doi.org/10.1128/jvi.01762-23>]). Thus, V591 was taken forward into phase I/II clinical trials in August 2020. Unexpected low immunogenicity in humans (O. Launay, C. Artaud, M. Lachâtre, M. Ait-Ahmed, J. Klein et al., *eBioMedicine* 75:103810, 2022, <https://doi.org/10.1016/j.ebiom.2021.103810>) revealed that the underlying mechanisms for resistance or sensitivity to pre-existing anti-measles immunity are not yet understood. Different hypotheses are discussed here, which will be important to investigate for further development of the measles-vectored vaccine platform.

**IMPORTANCE** SARS-CoV-2 emerged at the end of 2019 and rapidly spread worldwide causing the COVID-19 pandemic that urgently called for vaccines. We developed a vaccine candidate using the highly efficacious measles vaccine as vector, a technology which has proved highly promising in clinical trials for other pathogens. We report here and in the companion article by Nambulli et al. (*J Virol* 98:e01762-23, 2024, <https://doi.org/10.1128/jvi.01762-23>) the design, selection, and preclinical efficacy of the V591 vaccine candidate that was moved into clinical development in August 2020, 7 months after the identification of SARS-CoV-2 in Wuhan. These unique in-human trials of a measles vector-based COVID-19 vaccine revealed insufficient immunogenicity, which may be the consequence of previous exposure to the pediatric measles vaccine. The three studies together in mice, primates, and humans provide a unique insight into the

**Editor** Rebecca Ellis Dutch, University of Kentucky College of Medicine, Lexington, Kentucky, USA

Address correspondence to Nicolas Escriou, [nicolas.escriou@pasteur.fr](mailto:nicolas.escriou@pasteur.fr), or Annette Martin, [annette.martin@pasteur.fr](mailto:annette.martin@pasteur.fr).

Jérémy Brunet, Zaineb Choucha, and Marion Gransagne contributed equally to this article. Author order was determined alphabetically.

Christiane Gerke, Annette Martin, and Nicolas Escriou contributed equally to this article.

J. Brunet, Z.C., M.G., H.S.-M., M.M., P.C., L. Majlessi, C.G., A.M., and N.E. are inventors of a patent application describing measles-vectored vaccine candidates against SARS-CoV-2. All other authors declare no financial or non-financial competing interests.

See the funding table on p. 34.

See the companion article at <https://doi.org/10.1128/jvi.01762-23>.

**Received** 10 November 2023

**Accepted** 10 March 2024

**Published** 2 April 2024

Copyright © 2024 American Society for Microbiology. All Rights Reserved.

measles-vectored vaccine platform, raising potential limitations of surrogate preclinical models and calling for further refinement of the platform.

**KEYWORDS** COVID-19 vaccine, prefusion-stabilized spike, measles vector, vectored vaccine

Human severe acute respiratory syndrome coronavirus 2 (SARS-CoV-2) emerged in the province of Hubei in China at the end of 2019 (1, 2) and has rapidly spread worldwide causing the coronavirus disease 19 (COVID-19) pandemic with over 764 million confirmed cases and over 6.9 million reported deaths as of 5 May 2023 (3), when WHO declared the end of the health emergency status (4). Fifty vaccines were approved for use at the end of year 2022, based on mRNA, adenovirus vectorization technologies, inactivated virus, subunit strategies, or DNA (5), and 13 vaccines are currently granted Emergency Use Listing by WHO (6). They have played an undoubted essential role in containing the pandemic escalation, as well as in the current gradual transition to an endemic situation (7).

SARS-CoV-2 has posed an alarming health threat, in contrast to the phylogenetically related, highly pathogenic, yet distinct beta coronaviruses identified in humans during the past two decades: the first coronavirus associated to severe acute respiratory syndrome (SARS-CoV) (8, 9), which emerged in 2002 in China and caused an outbreak confined in time, and the Middle Eastern respiratory syndrome coronavirus (MERS-CoV) (10, 11), which emerged in 2012 in Saudi Arabia and remained geographically constrained and largely limited to zoonotic infection. Similar to other coronaviruses, SARS-CoV-2 is an enveloped, positive-stranded RNA virus, whose replication takes place in the cytoplasm of infected cells. Viral particles are composed of four major structural proteins, the nucleoprotein (N), the small envelope protein (E), the membrane protein (M), and the large spike protein (S). The spike protein is critical for virus cell entry [reviewed in reference (12)]. It is a type-I transmembrane glycoprotein of 1,273 amino acids, which assembles into homotrimers at the surface of viral particles giving the virion its crown-like appearance. Each spike monomer (180 kDa) is composed of an N-terminal signal sequence, followed by a large, highly glycosylated ectodomain, a transmembrane domain, and a short cytoplasmic tail (13–15). During biosynthesis of the S protein within the infected cell, the N-terminal signal sequence is cleaved off following endoplasmic reticulum (ER) insertion, and the resulting polypeptide is cleaved into S1 and S2 subunits by proprotein convertases of the host secretory pathway such as furin at a multibasic cleavage site. This site was not present in the spike protein of SARS-CoV (16) but was found important for cell entry of MERS-CoV (17). Non-covalently linked S1 and S2 subunits are assembled on mature viral particles. The S1 subunit carries the receptor-binding domain which binds human angiotensin-converting enzyme 2 (hACE2), and the S2 transmembrane subunit contains the fusion machinery. Receptor hACE2 engagement exposes an additional internal site within S2 subunit, the S2' site, which is cleaved by transmembrane protease serine 2 (TMPRSS2) in lung cells, a process that triggers a series of conformational changes, leads to the shedding of the S1 subunit and release of the fusion peptide from its buried position, and activates subsequent fusion between viral and cellular membranes (16, 18–20).

The humoral immune response to SARS-CoV-2 infection is mediated by antibodies elicited mostly against the structural S and N proteins, including neutralizing antibodies directed against S identified in naturally infected COVID-19 patients (21, 22). There is strong evidence for a protective role of neutralizing serum antibodies, although SARS-CoV-2-specific T and B cell memory certainly contributes some degree of protection (23, 24). Prior efforts from us and others in preclinical vaccine development for the related SARS-CoV and MERS-CoV have also established the spike protein as an essential vaccine target (25–28). Along these lines, the COVID-19 vaccines currently in

use target the spike protein and induce neutralizing antibodies and virus-specific T cell responses in vaccinated individuals [reviewed in references (29, 30)].

From the day the sequence of SARS-CoV-2 was available in January 2020, we launched our effort on the development of a replicating viral vector vaccine. Our approach was based on the measles vector (31, 32) as a clinical phase II-proven vaccine platform with demonstrated safety and high immunogenicity (33, 34) and our prior experience with SARS-CoV (26). We notably demonstrated that live-attenuated measles virus (MV) used as a vector for the native SARS-CoV spike (MV-SARS-CoV) induced strong humoral immune responses and full protection in susceptible mouse models (26). Replicating viral vector-based vaccines are particularly attractive for mass vaccination as they may induce strong and long-lasting immunity after only one or two injections and are compatible with low-cost manufacturing processes and large-scale vaccine deployment needed to control the COVID-19 pandemic. As such, the measles vaccine induces both efficacious humoral and cellular immune responses, has an excellent safety record, and provides durable protection (35). The most advanced measles vector-based vaccine candidate to date, a candidate against chikungunya virus (CHIKV), developed using the same measles Schwarz platform (MV-CHIK), has shown to be well tolerated and highly immunogenic in phase I and II clinical trials (34, 36). Importantly, a single dose resulted in seroconversion in approximately 90% of subjects receiving the highest tested dose levels, highlighting that one dose might be sufficient to gain clinical benefit which is crucial in a pandemic.

In the present study performed in the first half of 2020, we evaluated recombinant measles vectors expressing the native spike glycoprotein of SARS-CoV-2 or modified versions of this glycoprotein relying on prefusion stabilization of the spike and/or inactivation of the furin cleavage site (FCS). Our various recombinant vectors proved highly immunogenic and conferred protection against intranasal challenge with SARS-CoV-2 in susceptible mouse models. These preclinical studies allowed in June 2020 the selection of the most potent MV-SARS-CoV-2 vaccine candidate (MV-ATU3-S2PΔF2A, named V591) that was further brought to phase I/II clinical studies in August 2020 in parallel to its evaluation in non-human primates (NHP) (see companion article by Nambulli et al. [37]). In spite of its protective efficacy in both preclinical models following challenge with an early pandemic isolate of SARS-CoV-2, the immunogenicity of the selected V591 candidate in humans was low leading to discontinuation of further development (38, 39). Hypotheses for these discrepant findings and their importance for the future development of the measles vaccine platform are discussed.

## RESULTS

### Production and characterization of MV-SARS-CoV-2 recombinant viruses encoding native spike protein

For SARS-CoV, we previously showed that the membrane-anchored, full-length spike (S) protein was the most potent antigen when expressed from the measles vector (26). It induced the highest level of neutralizing antibodies and full protection from challenge with SARS-CoV in a susceptible murine model. Likewise, the membrane-anchored, full-length S protein of SARS-CoV-2 was chosen as antigen for the development of a measles-vectored vaccine against SARS-CoV-2. The spike nucleotide sequence was optimized both for transcription by MV vector and for translation in human cells. This codon-optimized sequence of S was introduced into either additional transcription unit (ATU) 2 (between MV phosphoprotein P and matrix M genes) or ATU3 (between MV hemagglutinin H and polymerase L genes) within a cDNA corresponding to the anti-genome of the MV Schwarz (MVSchw) vector (Fig. 1A, and Materials and Methods). Corresponding MV-ATU2-S and MV-ATU3-S were successfully rescued as described in Materials and Methods. Ten viral clones were individually expanded in Vero NK cells for each of ATU2-S and ATU3-S recombinant viruses to collect P0 viral stocks, whose infectivity was determined by endpoint dilution titration.

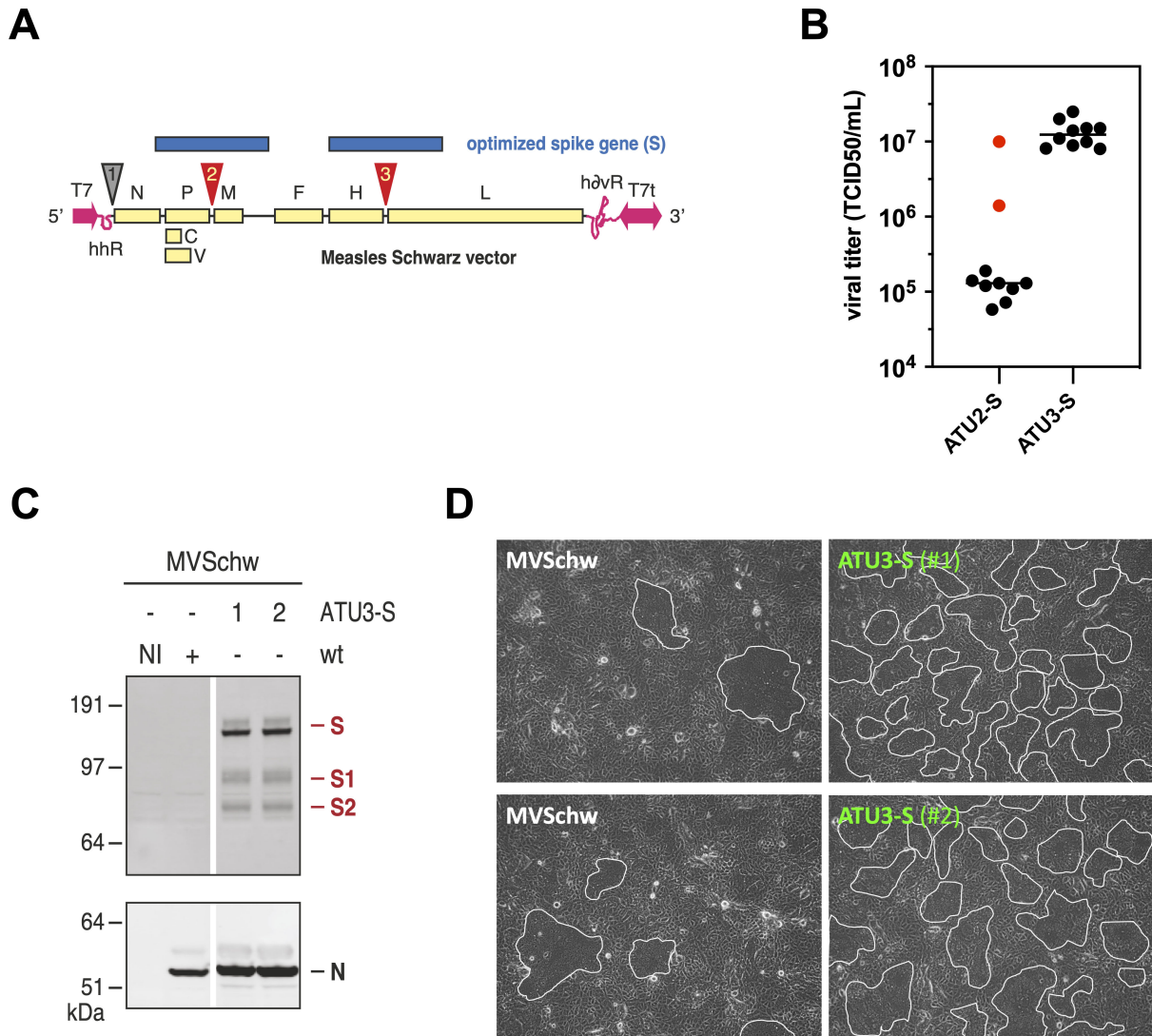


**FIG 1** Production and characterization of MV-SARS-CoV-2 recombinant viruses expressing native SARS-CoV-2 spike protein from either ATU2 or ATU3 site. (A) Schematic representation of SARS-CoV-2 spike sequence (blue box) inserted as an additional transcription unit at either the ATU2 or the ATU3 position (represented by red triangles) of the Measles virus Schwarz vector (underneath). MV anti-genome is cloned downstream of T7 RNA polymerase promoter (T7) and framed at its 5' end by hammerhead ribozyme (hhR) and at its 3' end by hepatitis delta virus ribozyme (hδvR) followed by T7 RNA polymerase terminator (T7t). MV-encoded proteins are indicated: N (nucleoprotein), P (phosphoprotein), C and V accessory proteins, M (matrix protein), F (fusion protein), H (hemagglutinin), and L (polymerase). (B) Viral production obtained from cells infected with MV-ATU2-S and MV-ATU3-S recombinants. The plot shows infectious titers (TCID<sub>50</sub>/mL) of P0 viral stocks obtained for 10 viral clones randomly selected from 2 independent rescue experiments and expanded. Red dots point to outlier viruses with unexpectedly high titers compared to mean titers obtained for the other MV-ATU2-S recombinants. Bars show medians. (C) Cells were infected at an MOI of 0.05 TCID<sub>50</sub>/cell with two viral clones (# 1, 2) of recombinant MV-ATU3-S or the parental MVSchw or were not infected (NI). Protein extracts collected at 39 h post-infection were analyzed by Western blot and probed with anti-SARS-CoV spike polyclonal rabbit antibodies (upper panel) and anti-MV nucleoprotein polyclonal rabbit antibodies (lower panel). The left and right part of each panel are from the same membrane (unnecessary in-between lanes have been removed). The positions of SARS-CoV-2 native S, S1, and S2 cleaved products, and MV N protein are shown with respect to molecular weight markers (in kilodalton). (D) Images of cell monolayers infected at an MOI of 0.05 TCID<sub>50</sub>/cell with MV-ATU3-S (clones # 1, 2) or the parental MVSchw and observed at 39 h post-infection. Areas of fused cells are highlighted by white frames.

All clones of MV-ATU3-S recombinant virus grew to similarly high titers of approximately 10<sup>7</sup> 50% tissue culture infectious dose (TCID<sub>50</sub>)/mL (Fig. 1B). In contrast, most recombinant MV clones expressing SARS-CoV-2 S from ATU2 grew to approximately 100-fold lower titers with the notable exception of two viral clones yielding titers in the 10<sup>6</sup>–10<sup>7</sup> TCID<sub>50</sub>/mL range (Fig. 1B, red dots). Viral genetic stability was checked by

Sanger sequencing of the entire ATUs for 10 viral clones retrieved following transfection. While all MV-ATU3-S recombinants harbored the input S sequence, the two MV-ATU2-S with higher infectious titers harbored mutations or insertions/deletions in the phosphoprotein gene sequence (gene end and/or gene junction) which immediately precedes the spike transgene. Noticeably, one of the two clones had a compensating frameshift deletion in the spike transgene and five quasi-species missense substitutions compatible with ADAR-mediated RNA editing. Upon subsequent passage (P1) of the ATU2-S viruses with initial low titers, whenever infectious titers reached high levels, viruses were found to contain multiple quasi-species substitutions including nonsense substitutions in the inserted S sequence. In contrast, the sequence of two randomly selected MV-ATU3-S clones was shown to be stable following further passage (P1) by next-generation sequencing (NGS) analysis of the full-length genome. These results indicate that the fully codon-optimized S gene generates unstable MV recombinants when inserted into position ATU2. Consequently, MV vectors with S inserted into ATU2 were not taken forward.

Spike expression in MV-ATU3-S-infected Vero cells was confirmed by Western blot analysis of cell lysates using polyclonal rabbit antisera raised against recombinant S protein of SARS-CoV (26, 40), which cross-reacted with SARS-CoV-2 S antigen. As shown in Fig. 1C (upper panel), a major product with the expected apparent molecular mass of 170 kDa corresponding to full-length S was expressed in similar amounts by two representative viral clones. Additional products with apparent molecular masses of 90 and 80 kDa, respectively, were also detected, demonstrating that S was partially cleaved into its S1 and S2 subdomains. Upon infection of Vero cells, the MVSchw parent typically induces the formation of multinucleated cells or syncytia as the result of the interaction between MV fusion (F) and attachment (H) glycoproteins and the host cell plasma membrane. Small syncytia formed initially fuse together progressively, resulting in a few wide areas of fused cells at 39 h post-infection (p.i.) (Fig. 1D, left panels). Comparatively, at the same time point after infection, a strikingly increased number of large syncytia were formed in cells infected with any of the two MV-ATU3-S clones assayed (Fig. 1D, right panels). This enhanced spread of MV-ATU3-S in Vero cell monolayers was extremely reproducible and was supported by increased production of measles nucleoprotein (N) in the corresponding cell lysates as compared to lysates prepared from MVSchw-infected monolayers (Fig. 1C, lower panel). The fusogenic phenotype of MV-ATU3-S suggested that native spike was expressed at the surface of infected cells and was functional, thus able to interact with the angiotensin-converting enzyme 2 (ACE2) receptor present on neighboring cells and to promote cell fusion. This enhanced SARS-CoV-2 S-driven fusogenic phenotype was considered a potential safety concern and risk for developing the vaccine. To address this concern, prefusion-stabilized forms of the spike antigen were introduced into the MV genome.

### **MV-SARS-CoV-2 recombinant viruses encoding stabilized spike variants in ATU3 are highly replicative, genetically stable, and lack fusogenic phenotype**

We, therefore, designed a series of constructs with two complementary approaches aiming at stabilizing SARS-CoV-2 spike protein in a prefusion conformation. Prefusion-locked spike protein was also expected to elicit higher relevant antibody responses, by analogy to what was observed for F protein of respiratory syncytial virus (41) and S protein of MERS-CoV (42). One approach relied on the substitution of two residues at positions 986 and 987 by proline residues (K986P + V987P, referred to as 2P), by analogy with modifications introduced into the spike sequence of SARS-CoV and MERS-CoV (42, 43). Another approach was to inactivate cleavage at the S1/S2 junction either through the substitution of the three arginine residues at positions 682, 683, and 685, comprising the multibasic cleavage site (R682G + R683S + R685G, referred to as 3F), or the deletion of the entire disordered solvent-exposed loop (14) encompassing the cleavage site (residues at positions 675 through 685, referred to as  $\Delta$ F) (Fig. 2A). We chose to compare the most straightforward 3F mutation approach to the loop deletion ( $\Delta$ F) as an attempt

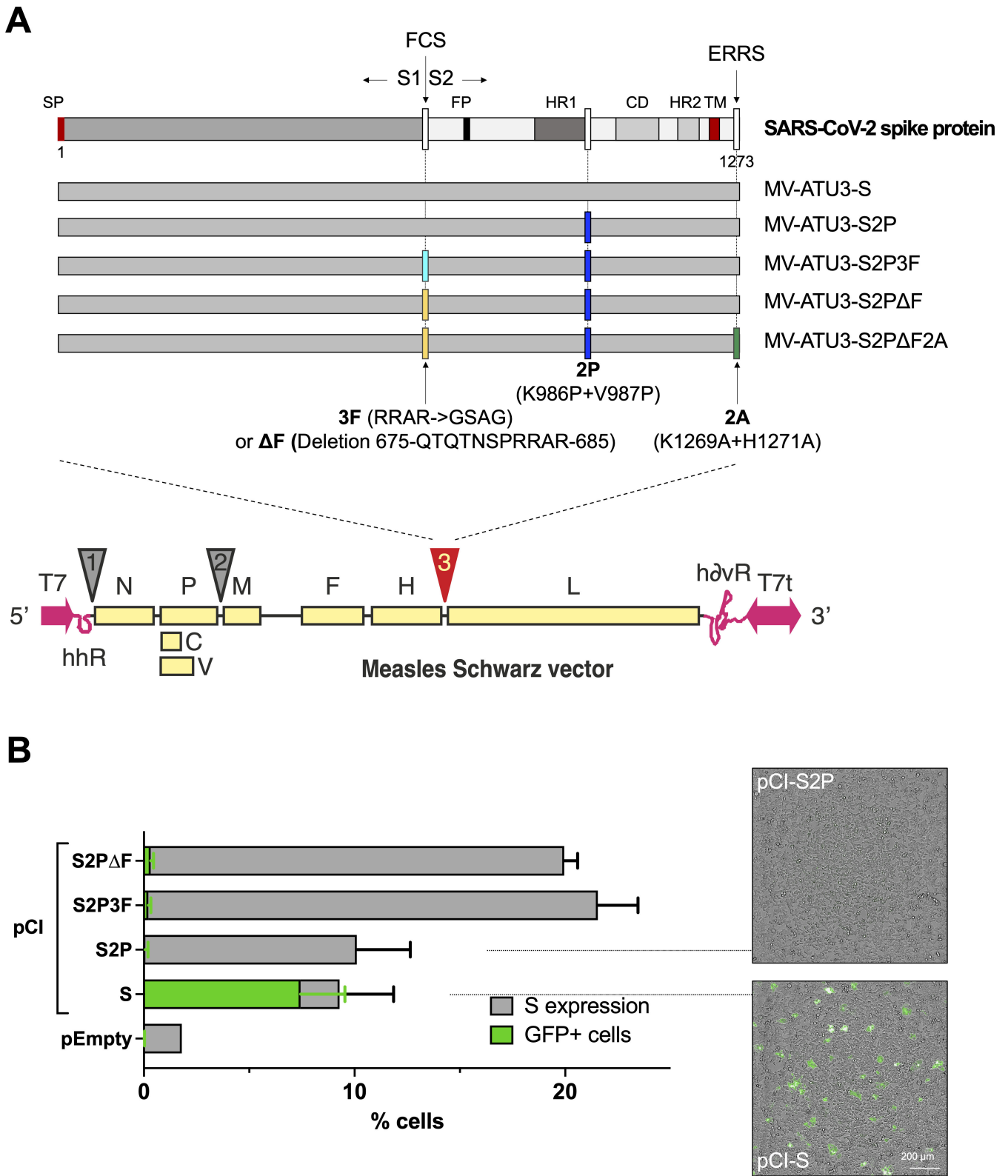


**FIG 2** Fusion properties of various SARS-CoV-2 spike mutants encoded by MV-ATU3 recombinants. (A) Schematic representation of the primary structure of SARS-CoV-2 spike protein, which comprises a signal peptide (SP) and two subdomains, S1 and S2, separated by an FCS. In the S2 domain, the fusion peptide (FP), heptad repeats (HR) 1 and 2, connector domain (CD), transmembrane domain (TM), and C-terminal endoplasmic reticulum retrieval signal (ERRS) are shown. Positions and combinations of mutations introduced into S sequence (2P, 3F, ΔF, 2A) are indicated below the schemes in yellow, cyan, blue, and green, (Continued on next page)

**FIG 2** (Continued)

respectively, and described by the position and nature of the resulting amino acid changes. Mutated S sequences were all inserted in the pCI mammalian expression vector and in ATU3 of Measles Schwarz vector, as illustrated at the bottom of the panel. (B) Fusion activities of native S and mutated S proteins were measured in transfected HEK-293T cells using split-GFP system in the presence of hACE2 and TMPRSS2 protease. Cells transfected with an empty plasmid (pEmpty) provided a negative control. Images of the cell monolayers (examples shown on the right) were analyzed at 18 h post-transfection. Percentages of cells expressing the indicated native or mutated S, and percentages of cells exhibiting GFP, scored as GFP areas per cell area, are plotted as means  $\pm$  SD from duplicates.

not only to bring further stiffness to the spike by the removal of the disordered loop but also to render the shortened peptide loop less accessible to other host proteases that could substitute for furin. Mammalian expression plasmids encoding spike variants with either 2P or combinations of 2P3F and 2P $\Delta$ F mutations were generated. Whether spike variants promote cell fusion was first evaluated in a transient cell fusion assay developed by Buchrieser et al. (44). This assay is based on the co-culture of HEK-293T cells stably expressing either of the two split-GFP fragments, which are co-transfected by plasmid DNAs allowing expression of hACE2 SARS-CoV-2 receptor, TMPRSS2 protease, and either native S or each of the S variants. GFP expression in fused cells was only detected if S was expressed at the surface of transfected cells and could trigger fusion with the neighboring cell expressing hACE2 receptor at its surface, a feature enhanced by the presence of TMPRSS2 protease. Data showed that the spike protein harboring either the stabilizing 2P mutation alone or combinations of the 2P mutation with the 3F mutation or  $\Delta$ F deletion inactivating S1/S2 cleavage did not induce fusion in this system, in contrast to the native spike (Fig. 2B, GFP-positive cell scoring). Of note, percentages of S-expressing cells were higher for the 2P3F and 2P $\Delta$ F variants than for native S or the 2P variant (Fig. 2B, S expression scoring).

Based on these results, recombinant measles vector genomes encoding spike variants bearing the 2P substitution alone or combinations of 2P and 3F mutations or  $\Delta$ F deletion were engineered in ATU3. In SARS-CoV, alteration of spike C-terminal ER retrieval signal (ERRS) was found to affect spike cell surface location upon co-expression with M protein but to only marginally alter spike subcellular localization and cell surface expression when the spike protein was expressed on its own (45). To investigate the putative benefit of altering the equivalent ERRS in SARS-CoV-2 spike expressed from MV, a combination of the 2P and  $\Delta$ F modifications together with substitution of codons at positions 1269 and 1271 by alanine codons (K1269A + H1271A, referred to as 2A) (see Fig. 2A) was engineered. Corresponding recombinants MV-ATU3-S2P, MV-ATU3-S2P3F, MV-ATU3-S2P $\Delta$ F, and MV-ATU3-S2P $\Delta$ F2A were successfully rescued, yielding in all cases high-titered P0 viral stocks, in the  $10^7$  TCID<sub>50</sub>/mL range. NGS sequencing of the full-length viral genomes confirmed the expected sequences with no significant quasi-species, with the exception of a silent mutation in the L gene of one viral clone of MV-ATU3-S2P $\Delta$ F2A. Importantly, comparative infection of cells with these viruses revealed slightly delayed to similar syncytia formation rate and expansion as that of the parental MVSchw, confirming absence of enhanced fusogenic activity, in contrast to MV-ATU3-S (Fig. 3A).

Time-course growth experiments showed that the replication of all MV-ATU3 recombinant viruses expressing prefusion-locked spike was slightly delayed at 24 h p.i. compared to parental MVSchw but reached similar peak titers of approximately  $10^7$  TCID<sub>50</sub>/mL at 48 h p.i. and thereafter (Fig. 3B). Of note, titers of MV expressing native S (MV-ATU3-S) peaked similarly at 48 h p.i. with a slightly higher titer than viruses expressing prefusion-locked spike but subsequently declined by about 10-fold at 60 h p.i., as a probable consequence of greater expansion of fused cell areas followed by extensive cytopathic effect (CPE) in the MV-ATU3-S infected cell monolayer. The genetic stability of the four viruses harboring the 2P stabilizing mutation and of MV-ATU3-S was confirmed after five passages in cell culture by Sanger sequencing of the ATU and NGS sequencing of the full-length viral genome.

Analysis of proteins extracted from cells infected at multiplicity of infection (MOI) of 1 with the various MV recombinants by Western blot using rabbit polyclonal antisera raised

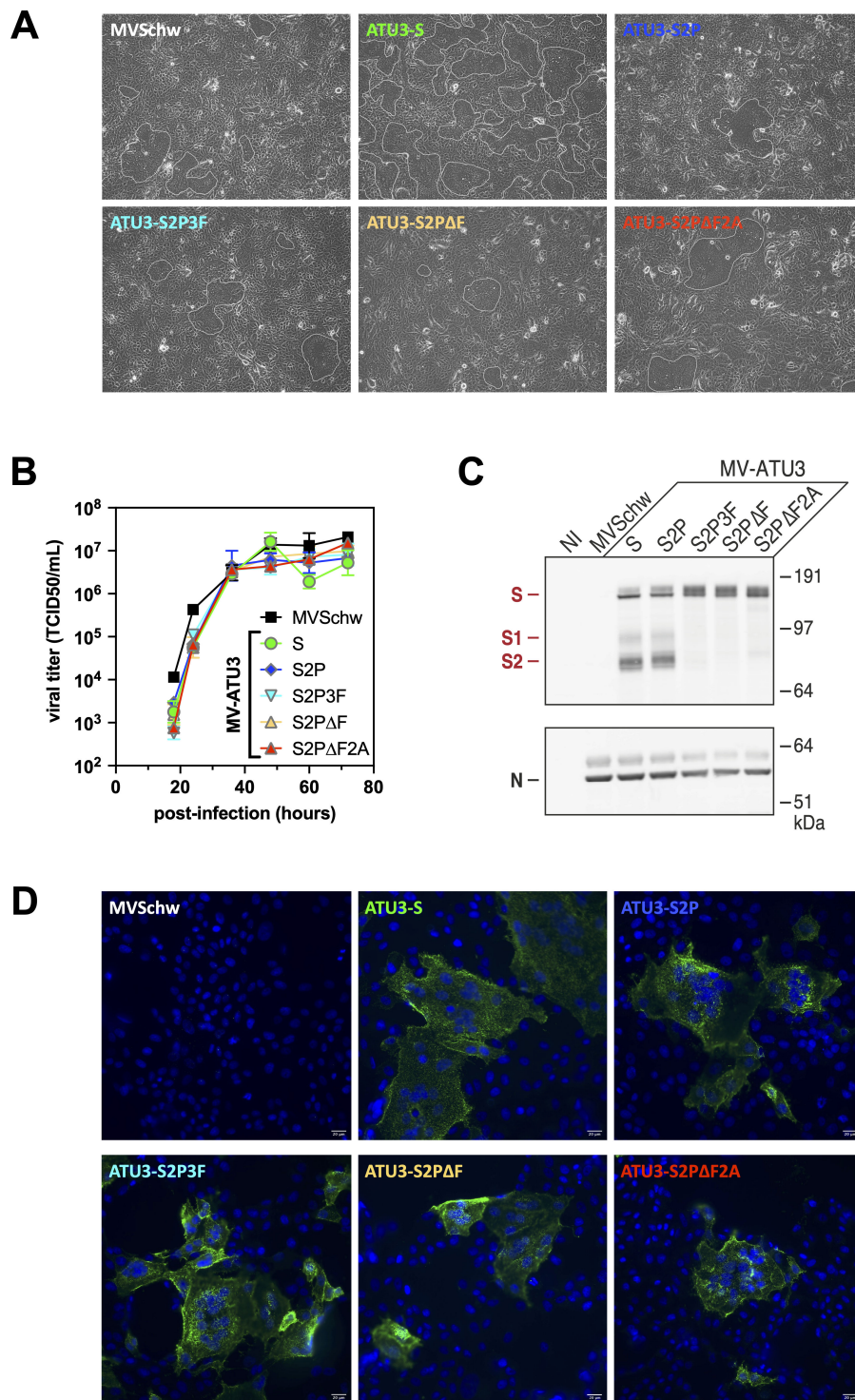


**FIG 3** Comparative characterization of measles vectors expressing various SARS-CoV-2 S mutants. (A) Images of cell monolayers infected at an MOI of 0.05 TCID<sub>50</sub>/cell with MV-ATU3 expressing the indicated native or mutated S or with parental MV-Schw and observed at 39 h post-infection. Areas of fused cells are highlighted by white frames. (B) Viral growth curves were established following infection of cells with recombinant MV-ATU3 expressing the indicated native or mutated S or with parental MV-Schw at an MOI of 0.05. Cell-associated viral titers were determined in cell cultures collected at the indicated times post-infection. Geometric means of duplicate experiments are presented, and error bars indicate geometric SD. (C) Cells were infected at an MOI of 1 with the indicated recombinant MV, or the parental MV-Schw, or were not infected (NI). Protein extracts collected at 24 h post-infection were analyzed by Western blot and probed with anti-SARS-CoV-2 spike (Continued on next page)

**FIG 3** (Continued)

polyclonal rabbit antibodies (upper panel) and anti-MV nucleoprotein antibodies (lower panel). The positions of SARS-CoV-2 full-length S, S1, and S2 domains, and MV N protein are shown with respect to molecular weight markers (in kilodalton). (D) Cell monolayers infected at an MOI of 0.05 with the same viruses as in (A) were fixed at 30 h post-infection and processed without permeabilization for indirect immunofluorescence with anti-SARS-CoV-2 spike polyclonal rabbit antibodies and AF488-conjugated anti-rabbit IgG antibodies. Cell nuclei were counterstained with DAPI. Representative Z-projection images recorded with a 40× objective are shown. Bar, 20 μm.

against SARS-CoV-2 spike ectodomain demonstrated efficient expression of full-length S in all cases (Fig. 3C, upper panel). Partial cleavage of S into its S1 and S2 subdomains occurred in MV-ATU3-S2P-infected cells, as in cells infected with MV expressing native S. Noteworthy, no difference in SARS-CoV-2 S and control measles N expression levels was observed in cells infected with MV-ATU3-S or MV-ATU3-S2P under such a single cycle of viral replication (at 24 h p.i., Fig. 3C, lower panel). Inactivation of the furin cleavage site either by the 3F mutation (MV-ATU3-S2P3F) or the ΔF deletion (MV-ATU3-S2PΔF, MV-ATU3-S2PΔF2A) abolished S cleavage, as expected, and did not have any apparent significant impact on S expression levels. In addition, expression of spike was readily detected by indirect immunofluorescence of non-permeabilized syncytia in infected cultures, indicating that native S and all mutated forms were transported to the cell surface (Fig. 3D).

**MV-ATU3 recombinant viruses expressing stabilized spike variants induce strong anti-SARS-CoV-2 neutralizing antibody responses**

The immunogenicity of MV-ATU3 candidates expressing native S or S derivatives was evaluated in genetically modified 129/Sv mice, deficient for type 1 interferon receptor (IFNAR-KO), a small animal model suitable for the assessment of measles-vectored vaccines (46). Groups of five to six 6–10-week-old IFNAR-KO mice were immunized twice at a 4-week interval with intraperitoneal injection of  $1 \times 10^5$  TCID<sub>50</sub> of each vaccine candidate. As a control, a group of mice injected with a similar dose of empty MVSchw vector was included in each experiment. Mouse sera were collected 3 weeks after the first (prime) and second (boost) injections in two independent sets of experiments involving one viral clone for MV-ATU3-S and -S2P and two viral clones for MV-ATU3-S2P3F, -S2PΔF, and -S2PΔF2A (Fig. 4).

To assess humoral responses, MV- and SARS-CoV-2-specific antibody responses were first evaluated by indirect ELISA against native MV antigens and recombinant SARS-CoV-2 trimeric spike ectodomain, respectively. Mice immunized with the different recombinant measles vectors expressing native or mutated SARS-CoV-2 spike or with MVSchw seroconverted to MV after prime immunization (Fig. 4A and D). Anti-MV antibody levels were in the same range for all tested MV recombinants and parental MVSchw, suggesting that expression of the heterologous S protein did not alter the replication of the recombinant viruses *in vivo* nor modify their measles-specific immunogenicity. A few mice responded poorly to the prime immunization but all did respond strongly after boost immunization. Of note, the anti-MV antibody levels increased after boost by about 10-fold, as expected from previous studies in mice (26, 46).

All mice immunized with MV-ATU3-S, MV-ATU3-S2P, MV-ATU3-S2P3F, MV-ATU3-S2PΔF, and MV-ATU3-S2PΔF2A that developed high titers of anti-measles antibodies also responded with high titers of spike-specific antibodies, in the  $10^4$  ELISA-unit range after prime, as measured by the ELISA specific for SARS-CoV-2 spike (Fig. 4B and E). In contrast, control mice immunized with empty MVSchw were all tested negative, as expected. Significantly higher anti-S antibody levels were elicited after prime by recombinant MV expressing S2P with inactivated furin cleavage site (MV-ATU3-S2P3F, MV-ATU3-S2PΔF) compared to those elicited by MV-ATU3-S or MV-ATU3-S2P (Fig. 4B). After boost, the anti-S antibody levels increased by at least 10-fold, as observed for anti-MV antibodies. A trend for higher anti-S antibody levels after boost, although less or no longer significant,

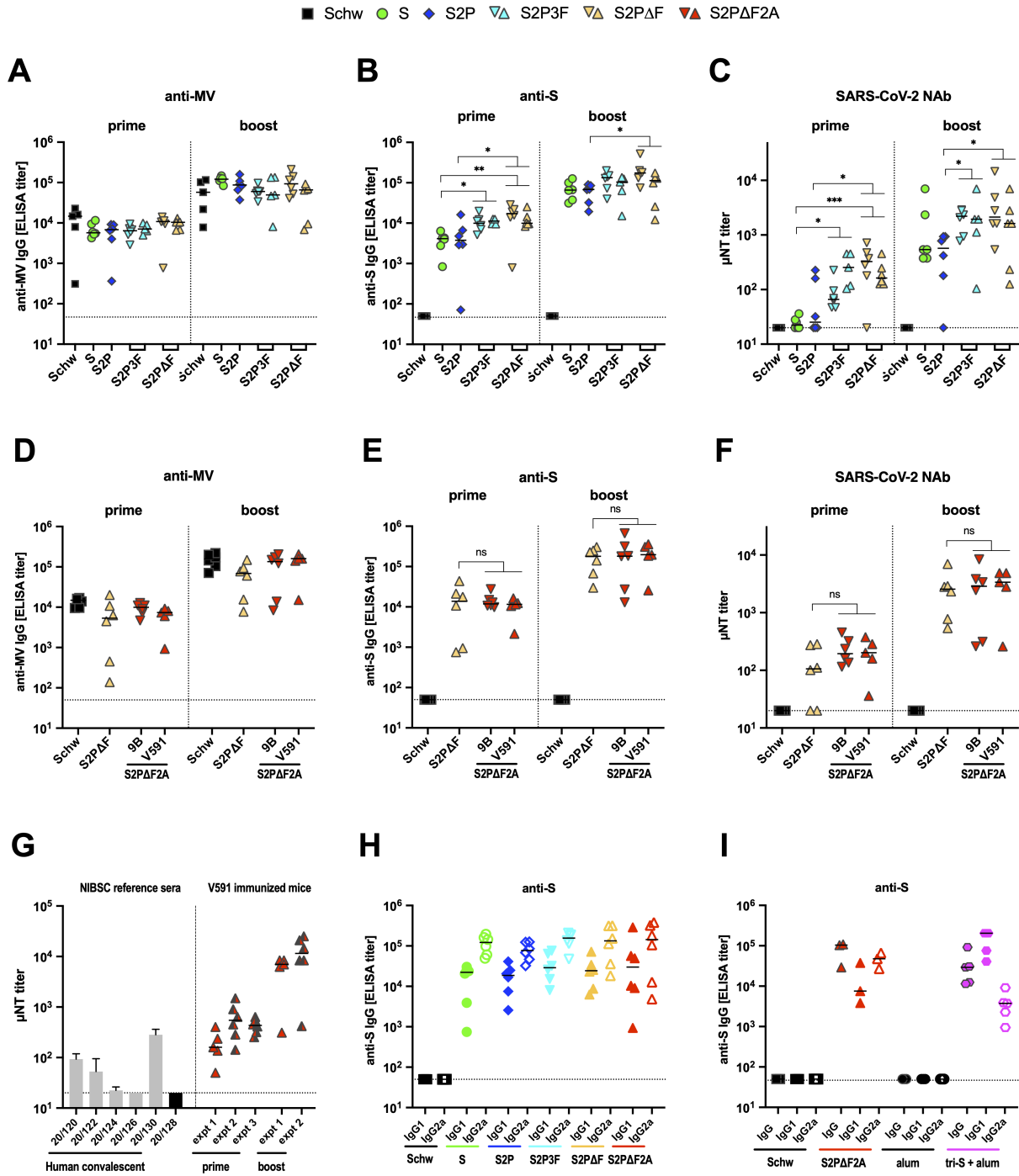


**FIG 4** Antibody responses in IFNAR-KO mice after prime and boost immunization with recombinant MV expressing SARS-CoV-2 native or mutated spike. (A–F) Mice ( $n = 6$  per group) were immunized with the parental MV Schwarz strain (Schw), one viral clone of MV-ATU3-S (S) and MV-ATU3-S2P (S2P), or either of two viral clones of MV-ATU3-S2P3F (S2P3F), MV-ATU3-S2PΔF (S2PΔF), and MV-ATU3-S2PΔF2A (S2PΔF2A). Antibody responses were measured by measles-specific ELISA (A, D), SARS-CoV-2 spike-specific ELISA (B, E), and SARS-CoV-2 microneutralization assay (C, F) in individual mouse sera collected following prime (left parts of the graphs) or boost (right parts of the graphs). Bars show medians. ELISA titers are expressed as reciprocals of endpoint serum dilutions. Neutralization titers are expressed as reciprocals of serum dilutions that resulted in the neutralization of 95% SARS-CoV-2 infectivity scored by cytopathic effect. Detection limits (dotted lines) in the anti-MV and anti-S ELISAs were 50 ELISA units and 20 in the microneutralization assay. Representative results of two or more independent experiments are shown. Statistical significance (B, C, E, F) was assessed using the non-parametric Kruskal-Wallis test with Dunn’s uncorrected post hoc analysis and is systematically indicated: \* $P < 0.05$ , \*\* $P < 0.005$ , \*\*\* $P < 0.0005$ . Statistical power of the analysis has been increased by running the values obtained in the same experiment for two clones of the same construct (S2P3F, S2PΔF, S2PΔF2A) against those obtained for each of the parental constructs (S, S2P).

(Continued on next page)

**FIG 4** (Continued)

Non-significance (ns) is indicated whenever referred to in the text. (G) Comparative assessment of the SARS-CoV-2 microneutralization titers of sera from mice immunized with MV-ATU3-S2PΔF2A in three independent experiments (expt 1, 2, 3) and convalescent human sera 20/120, /122, /124, /126, /130 or negative control human serum 20/128 provided by the National Institute of Biological Standards and Controls (NIBSC, UK). The results for NIBSC research reagents are plotted as geometric means with geometric SD error bars of the titers obtained in all microneutralization assays in which they were tested together with mouse sera. The results for individual mice are represented per immunization experiment. Bars show medians. (H, I) Total IgG or isotype-specific (IgG1 and IgG2a) antibody responses against SARS-CoV-2 spike were measured by ELISA using recombinant SARS-CoV-2 trimeric S ectodomain produced in mammalian (H) or insect (I) cells as coating antigen. Bars show medians. Detection limit was 50 ELISA units. For comparison of the IgG2a/IgG1 ratio elicited by recombinant MV expressing S, wild-type 129/Sv mice were immunized with aluminum-adsorbed trimerized spike ectodomain (tri-S + alum) produced in mammalian cells or aluminum adjuvant alone (alum).

was still detected in favor of recombinant MV expressing S2P3F or S2PΔF over those expressing S or S2P (Fig. 4B). We indeed reproducibly observed that lower responses after prime with MV-ATU3-S or S2P candidates were accompanied with higher boosting effect after the second injection than with MV-ATU3-S2P3F or MV-ATU3-S2PΔF (Fig. S1). We cannot rule out that there might be some kind of maximum antibody production level in mice that is more easily reached after immunization with furin-site inactivated mutants. However, it is interesting to note that a similar trend has been observed for adjuvanted spike vaccines bearing or not furin cleavage site inactivation in BALB/c mice (47).

The magnitude of anti-SARS-CoV-2 neutralizing antibody responses was quantified using a microneutralization assay and determined neutralizing titers as the reciprocal of the highest serum dilution required to reduce infection by authentic SARS-CoV-2 virions by 95% (NT95). All recombinant MV expressing SARS-CoV-2 S or S derivatives elicited neutralizing antibodies after one immunization, albeit only half of the mice had detectable neutralizing antibodies after prime with MV-ATU3-S or MV-ATU3-S2P (Fig. 4C). Importantly, significantly higher neutralizing titers were obtained following prime with MV-ATU3-S2P3F or MV-ATU3-S2PΔF (average  $\log_{10}$  titer of  $2.1 \pm 0.4$  and  $2.3 \pm 0.4$ , respectively) than with MV-ATU3-S ( $1.4 \pm 0.1 \log_{10}$ ) or MV-ATU3-S2P ( $1.7 \pm 0.5 \log_{10}$ ). Noticeably, there was a reproducible trend for induction of higher neutralizing titers after prime by MV-ATU3-S2PΔF over MV-ATU3-S2P3F, although the increase was not statistically significant by Kruskal-Wallis non-parametric test. In addition, there was no difference between SARS-CoV-2 ELISA and neutralizing titers reached after prime or boost immunization with MV-ATU3-S2PΔF2A and MV-ATU3-S2PΔF (Fig. 4E and F), indicating no role for the putative ERRS in the immunogenicity of the SARS-CoV-2 S protein in this context. After boost, neutralizing titers also increased by at least 10-fold. All three recombinant MV expressing SARS-CoV-2 S with inactivated furin cleavage site (MV-ATU3-S2P3F, -S2PΔF, -S2PΔF2A) elicited similar neutralizing antibody levels after boost that were again significantly higher than those obtained with MV-ATU3-S or MV-ATU3-S2P (Fig. 4C and F). Similar data obtained for two viral clones of each consolidated the superiority of the former three candidates in conferring the highest immunogenicity to SARS-CoV-2.

To evaluate the strength of the neutralizing antibody response induced in mice by MV-ATU3-S2PΔF2A, which proved to be one of the best candidates, individual mouse sera collected after prime and boost in this and in two other independent immunization experiments were subjected to microneutralization alongside a panel of six National Institute of Biological Standards and Controls (NIBSC) reference convalescent sera from COVID-19 patients, including low-titer (20/124, 20/126), medium-titer (20/122), high-titer (20/120), and very high-titer (20/130) sera (see description in the Materials and Methods). As shown in Fig. 4G, the vast majority of mouse sera after MV-ATU3-S2PΔF2A (clone V591) prime had neutralizing titers around or above those found in the high- to very high-titer 20/120 and 20/130 human convalescent sera and, after boost, exhibited titers at least 100-fold higher. These data underlined that MV-ATU3-S2PΔF2A was able to elicit a strong SARS-CoV-2 neutralizing response likely to be biologically meaningful. All following experiments were performed with the same V591 clone of MV-ATU3-S2PΔF2A.

## MV-ATU3 recombinant viruses expressing stabilized spike variants induce robust CD8<sup>+</sup> and Th1-biased CD4<sup>+</sup> T cell responses

Based on the recommendation of the International Coalition of Medicinal Regulatory Agencies (ICMRA) (48), it was important to ensure induction of a type 1 (Th1) response to mitigate the risk for potential disease enhancement that had been observed in animal models with SARS-CoV vaccine candidates (49). As IgG isotypes indicate potential skewing of the ongoing CD4<sup>+</sup> helper T cell response into a Th1 or type 2 (Th2) response in mice, we first measured the ratio of IgG2a to IgG1 antibody titers by isotype-specific anti-S ELISA. This analysis revealed that MV-ATU3-S, -S2P, -S2P3F, -S2PΔF, and -S2PΔF2A all induced higher IgG2a than IgG1 levels (Fig. 4H), indicating a predominant Th1 response, as expected from a live viral vector. To strengthen these data, control experiments were performed by immunizing wild-type 129/Sv mice with aluminum hydroxide-adjuvanted, recombinant trimeric spike ectodomain (50). After prime and boost with this subunit vaccine strategy, mice had substantially higher IgG1 than IgG2a antibody titers (Fig. 4I), indicating that the induced immune responses were predominantly of Th2 type, as previously observed by us after immunization with aluminum hydroxide-adjuvanted SARS-CoV spike ectodomain (26) and also reported by Corbett et al. (51) for SARS-CoV-2 spike. It was noteworthy in this experiment that prime with alum-adjuvanted recombinant spike did not induce detectable neutralizing antibodies in four out of five mice, whereas after boost, responses were in the low 10<sup>3</sup> range (average log<sub>10</sub> titer of 2.9 ± 0.6) and somehow weaker than those induced after prime and boost with MV-S2PΔF2A.

In order to directly measure and characterize T cell responses in more detail, including to confirm the type of T helper cell responses, S-specific T cell responses were analyzed in splenocytes from vaccinated mice by intracellular cytokine staining (ICS) and flow cytometry. IFNAR-KO mice were immunized twice at a 4-week interval with recombinant MV-ATU3-S, -S2P, -S2P3F, -S2PΔF, -S2PΔF2A, or with the parental MVSchw. Nineteen to 25 days after the boost immunization, splenocytes were stimulated with overlapping peptide pools spanning full-length S1 and S2 domains of the spike protein, respectively. As control, measles-specific responses were assessed using a pool of two peptides corresponding to H-2<sup>b</sup> immunodominant epitopes of hemagglutinin for CD8<sup>+</sup> T cells (52). In all mice immunized with any of the recombinant MV expressing SARS-CoV-2 S or S mutants, ICS of splenocytes detected CD4<sup>+</sup> T cells producing IFN-γ and/or TNF-α after stimulation with the spike peptide pools (Fig. 5A). The frequencies of all CD4<sup>+</sup> cells producing TNF-α (alone or in combination with IFN-γ) and of TNF-α/IFN-γ double-positive CD4<sup>+</sup> cells were significantly higher in mice immunized with any of the recombinant MV compared to mice immunized with the MVSchw. Particularly, the IFN-γ/TNF-α double-positive CD4<sup>+</sup> T cells were indicative of more differentiated polyfunctional CD4<sup>+</sup> T cells (53), confirming that S-specific Th1-type responses were induced by the vaccine candidates.

Further supporting the Th1 response, no S-specific CD4<sup>+</sup> T cells expressing both IL-5 and IL-13, characteristic for Th2 responses, were detected in mice receiving any of the recombinant MV (Fig. 5B). While a low frequency of cells producing IL-5 or IL-13 was detected in some animals immunized with the furin-site inactivated vectors, there was no statistical difference with the frequency of those cells in splenocytes from mice immunized with MVSchw, indicating that these responses were not specific for the S protein.

In accordance with the Th1 CD4<sup>+</sup> T cell response, a strong CD8<sup>+</sup> T cell response was induced (Fig. 5C). The frequencies of all S-specific CD8<sup>+</sup> T cells producing TNF-α, or IFN-γ, and of polyfunctional S-specific CD8<sup>+</sup> T cells producing both TNF-α and IFN-γ were significantly higher in mice immunized with any of the S-expressing recombinant MV compared to mice immunized with MVSchw. The frequencies of double-positive S-specific CD8<sup>+</sup> T cells were about three times as high as the frequencies of double-positive CD4<sup>+</sup> T cells (Fig. 5A and C). No significant IL-5 or IL-13 S-specific responses were observed in CD8<sup>+</sup> T cells either (Fig. 52).

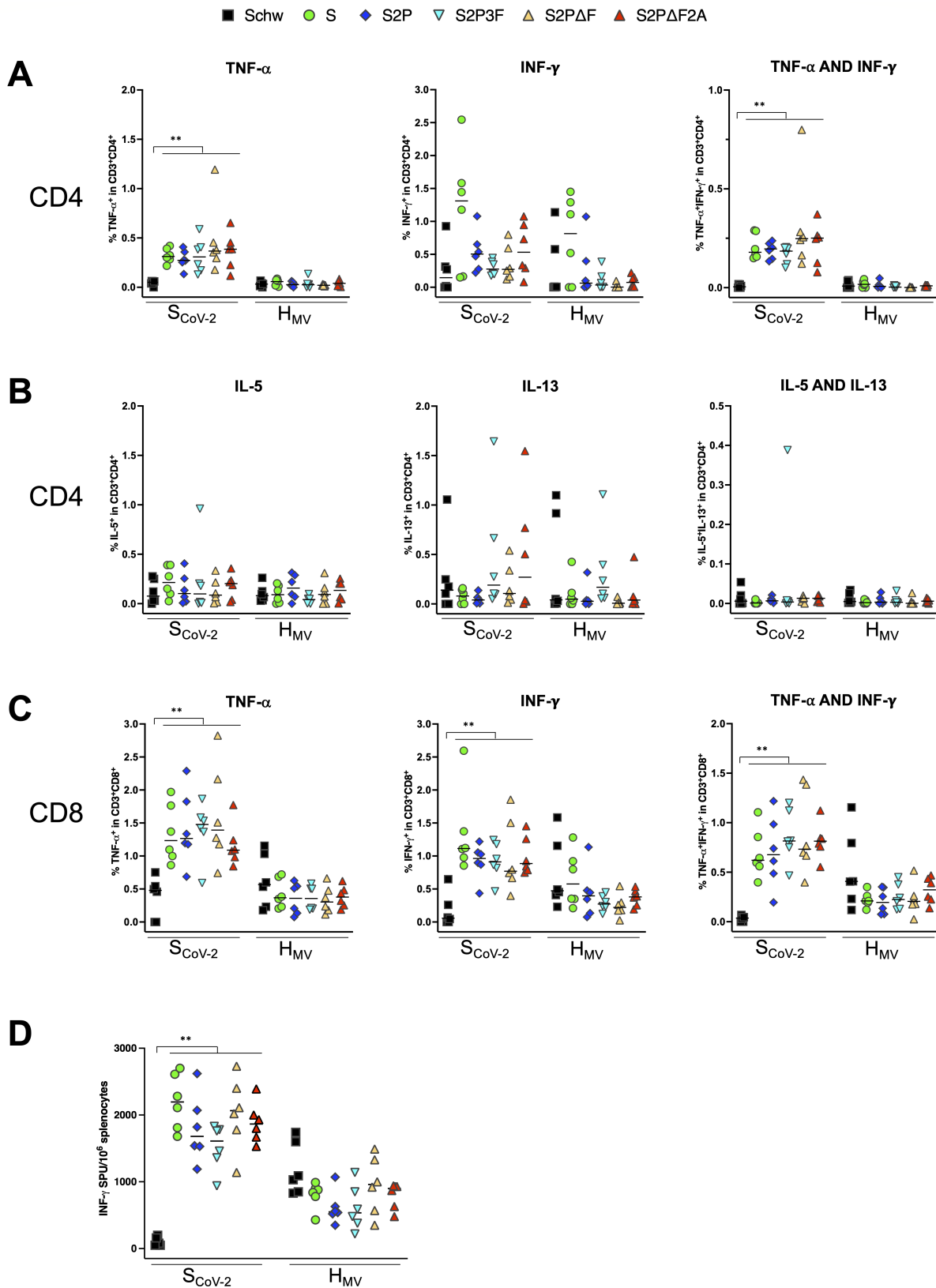


**FIG 5** MV and S-specific T cell responses in mice immunized with recombinant MV expressing SARS-CoV-2 native or mutated spike. Mice ( $n = 6$  per group) were immunized twice with MV-ATU3-S (S), MV-ATU3-S2P (S2P), MV-ATU3-S2P3F (S2P3F), MV-ATU3-S2PΔF (S2PΔF), MV-ATU3-S2PΔF2A (S2PΔF2A), or parental MV Schwarz (Schw). Splenocytes collected following boost were stimulated with peptide pools spanning the S1 or S2 domain of SARS-CoV-2 spike (summed) (Continued on next page)

**FIG 5** (Continued)

responses to S1 and S2 pools are shown: S<sub>CoV-2</sub>, left parts of the graphs) or a pool of two H-2<sup>b</sup> class I-restricted measles hemagglutinin peptides (H<sub>MV</sub>, right parts of the graphs). Frequencies of cytokine-producing cells determined by intracellular cytokine staining followed by flow cytometry are shown for (A) splenic CD4<sup>+</sup> T cells producing Th1 signature cytokines TNF- $\alpha$ , IFN- $\gamma$ , or both IFN- $\gamma$  and TNF- $\alpha$ , (B) splenic CD4<sup>+</sup> T cells producing Th2 signature cytokines IL-5, IL-13, or both IL-5 and IL-13, and (C) splenic CD8<sup>+</sup> T cells producing TNF- $\alpha$ , IFN- $\gamma$ , or both IFN- $\gamma$  and TNF- $\alpha$ . Frequencies of IFN- $\gamma$ -producing T cells were enumerated by ELISpot analysis and shown as spot forming units (SPU) per 10<sup>6</sup> cells (D). Bars show medians. Statistical significance was assessed using the non-parametric Kruskal-Wallis test with Dunn's uncorrected post hoc analysis:  $^{***}P < 0.005$ .

It is noteworthy that the frequencies of the S-specific CD4<sup>+</sup> and CD8<sup>+</sup> T cell responses induced after a booster administration were not statistically different for any of the recombinant MV expressing SARS-CoV-2 S or S mutants, in-line with anti-S antibody responses that tend to reach similar values after boost, as reported above.

Similar results were obtained when ICS was performed on splenocytes after stimulation with naturally processed spike antigen instead of synthetic peptide pools. Bone-marrow derived dendritic cells were loaded either with recombinant spike protein to detect CD4<sup>+</sup> T cells or by transduction with a lentiviral vector encoding full-length spike to detect CD8<sup>+</sup> T cells. This demonstrated the induction of S-specific CD4<sup>+</sup> and CD8<sup>+</sup> T cells producing TNF- $\alpha$  and IFN- $\gamma$  (Fig. S3A and C) but not IL-5 and IL-13 (Fig. S3B), further confirming the induction of Th1 responses by the vaccine candidates.

Furthermore, TNF- $\alpha$ - and/or IFN- $\gamma$ -positive CD8<sup>+</sup> T cells specific for measles vector backbone were confirmed in mice receiving any of the recombinant MV as well as in mice immunized with the parental MVSchw (Fig. 5C). However, in mice receiving any of the S expressing measles vector vaccine candidates, the frequency of the measles hemagglutinin-specific CD8<sup>+</sup> T cells (as measured against the two dominant peptides) was lower than the frequency of SARS-CoV-2 S-specific CD8<sup>+</sup> T cells, demonstrating the biological significance of the T cell responses induced against the expressed spike protein.

In addition to the ICS experiments, IFN- $\gamma$ -producing T cells were enumerated by ELISpot. The results confirmed the strong cellular responses against peptides spanning the S protein after immunization with all recombinant MV-expressing spike protein, with approximately 2,000 IFN- $\gamma$  spot-forming units (SPU) per 10<sup>6</sup> splenocytes (Fig. 5). Cellular responses to the measles vector hemagglutinin peptides were comparable after immunization with any of the recombinant MV and parental MVSchw, with approximately 1,000 IFN- $\gamma$  SPU/10<sup>6</sup> splenocytes (Fig. 5D).

Deconvolution of the peptide pools by ELISpot analyses revealed five immunodominant peptides which were further characterized by ICS (Fig. S4). One of the peptides (#13, S:61–75, NVTWFHAIHVSGTNG) was recognized by CD4<sup>+</sup> T cells, and four other peptides (#52, S:256–270, SGWTAGAAAYVGYL; #53, S:261–275, GAAAYVGYLQPRTF; #108, S:536–550, NKCVNFNFNGLTGTG; #116, S:576–590, VRDPQTLEILDITPC), of which two are overlapping and likely correspond to a single epitope (# 52 and 53), are recognized by CD8<sup>+</sup> T cells, as described by Ku et al. (54). Furthermore, comparison of ICS frequencies for CD8<sup>+</sup> T cells indicated that the S:536–550 peptide (#108) most likely contains the H-2<sup>b</sup> class I immunodominant epitope, in agreement with recently published data obtained in mice immunized with Venezuelan equine encephalitis replicon particles expressing SARS-CoV-2 S (55) and that S:256–270/S:261–275 (# 52 and 53) and S:576–590 (#116) contain two subdominant epitopes. Comparison of ICS frequencies for CD4<sup>+</sup> T cells suggested that the S:61–75 peptide (#13) contains a dominant epitope, confirming data reported by Zhuang et al. (55) but also that other epitope(s) likely contribute to the higher frequency of the response detected against the spike peptide pools.

## Immune responses induced by MV-ATU3 recombinant viruses expressing stabilized S variants protect against SARS-CoV-2 challenge, including after single immunization

To assess the potential of the recombinant MV-ATU3 expressing native S or S variants to induce protection against experimental challenge infection with SARS-CoV-2, we used IFNAR-KO mice in which the human ACE2 receptor of SARS-CoV-2 was transiently expressed in the pulmonary mucosa by transduction with an Ad5 gene transfer vector (Ad5::hACE2). Such pretreatment allows subsequent infection with SARS-CoV-2, and high rates of viral replication can be detected in the lungs (54, 56).

Protection was first monitored after prime and boost immunization with either MV-ATU3-S, MV-ATU3-S2P, MV-ATU3-S2PΔF, MV-ATU3-S2PΔF2A, or the parental MVSchw strain as control. Mice were instilled via intranasal (i.n.) administration with Ad5::hACE2 4 weeks after the boost immunization and inoculated i.n. with  $2 \times 10^4$  PFU of an early pandemic isolate of SARS-CoV-2 4 days later. We did not observe weight loss nor behavioral changes in control MVSchw-immunized mice inoculated with SARS-CoV-2, consistent with the findings reported by Rathnasinghe et al. (57). SARS-CoV-2 load in the lungs was assessed 4 days after challenge by RT-qPCR measuring genome equivalent (GEQ) RNA levels, as well as by quantification of infectious titers in Vero cells. As shown in Fig. 6A, a two-dose immunization at a 4-week interval with all measles vectors expressing S or S derivatives triggered a significant reduction in the lung SARS-CoV-2 load compared to immunization with MVSchw parental virus. Approximately 60-fold and 300- to 600-fold reductions in viral RNA levels were achieved following vaccination with MV-ATU3-S or MV-ATU3-S2P and MV-ATU3-S2PΔF or MV-ATU3-S2PΔF2A, respectively. Furthermore, no SARS-CoV-2 infectivity was detected in any of the mice immunized with MV-ATU3-S2P, MV-ATU3-S2PΔF, or MV-ATU3-S2PΔF2A. Only one mouse immunized with MV-ATU3-S, which had responded poorly to the immunization and had very low neutralizing antibody titers, showed low residual SARS-CoV-2 titers. Altogether, these results showed that vaccination with recombinant MV significantly reduced the viral load in the lungs of challenged animals and, particularly, that the production of infectious particles was prevented. Noteworthy, the efficiency of protection followed the hierarchy observed with the induction of neutralizing antibody levels, MV-ATU3-S2PΔF and MV-ATU3-S2PΔF2A conferring significantly better protection than MV-ATU3-S and MV-ATU3-S2P ( $P < 0.05$  using ANOVA and uncorrected Fisher's LSD test on pulmonary SARS-CoV-2 RNA levels).

Based on the promising results after prime and boost immunization, protection after prime only was assessed in mice immunized with MV-ATU3-S2PΔF2A, MV-ATU3-S2P, or the control parental MVSchw with challenge 5 weeks after immunization. Neutralizing antibody titers were higher in MV-ATU3-S2PΔF2A-immunized mice than in MV-ATU3-S2P-immunized animals 7 days prior to challenge (Fig. 6B), as observed in previous experiments (Fig. 4C). This translated into better protection with significantly lower SARS-CoV-2 RNA loads ( $P < 0.05$  using Mann-Whitney test) and absence of detectable infectious particles in the lungs for MV-ATU3-S2PΔF2A-immunized mice (Fig. 6B). These protection results were further strengthened by immunohistochemistry (IHC) analysis of the lungs of challenged animals, using a SARS-CoV-2 nucleocapsid protein (NCoV-2)-specific polyclonal antibody. In control MVSchw-immunized and SARS-CoV-2-infected mice, numerous foci of NCoV-2+ cells were detected in the bronchial epithelial cells and in the interstitium that were absent in mock-challenged mice (Fig. S5, left panels). Although some degree of intra-group and inter-lobe variation could be observed, IHC images displayed a markedly less abundant NCoV-2 staining in MV-ATU3-S2P- and MV-ATU3-S2PΔF2A-vaccinated animals (Fig. S5, right panels). NCoV-2-positive foci were counted in representative sections of all lobes (Fig. 6B, right panel). These data revealed that the lungs of MV-S2PΔF2A-vaccinated mice exhibited very few NCoV-2+ foci, if at all, while MV-S2P-vaccinated mice came up with low scores that were significantly different ( $P < 0.005$ ) from those obtained in MVSchw-vaccinated mice. The better protection conferred by MV-ATU3-S2PΔF2A with respect to MV-ATU3-S2P was statistically significant ( $P <$

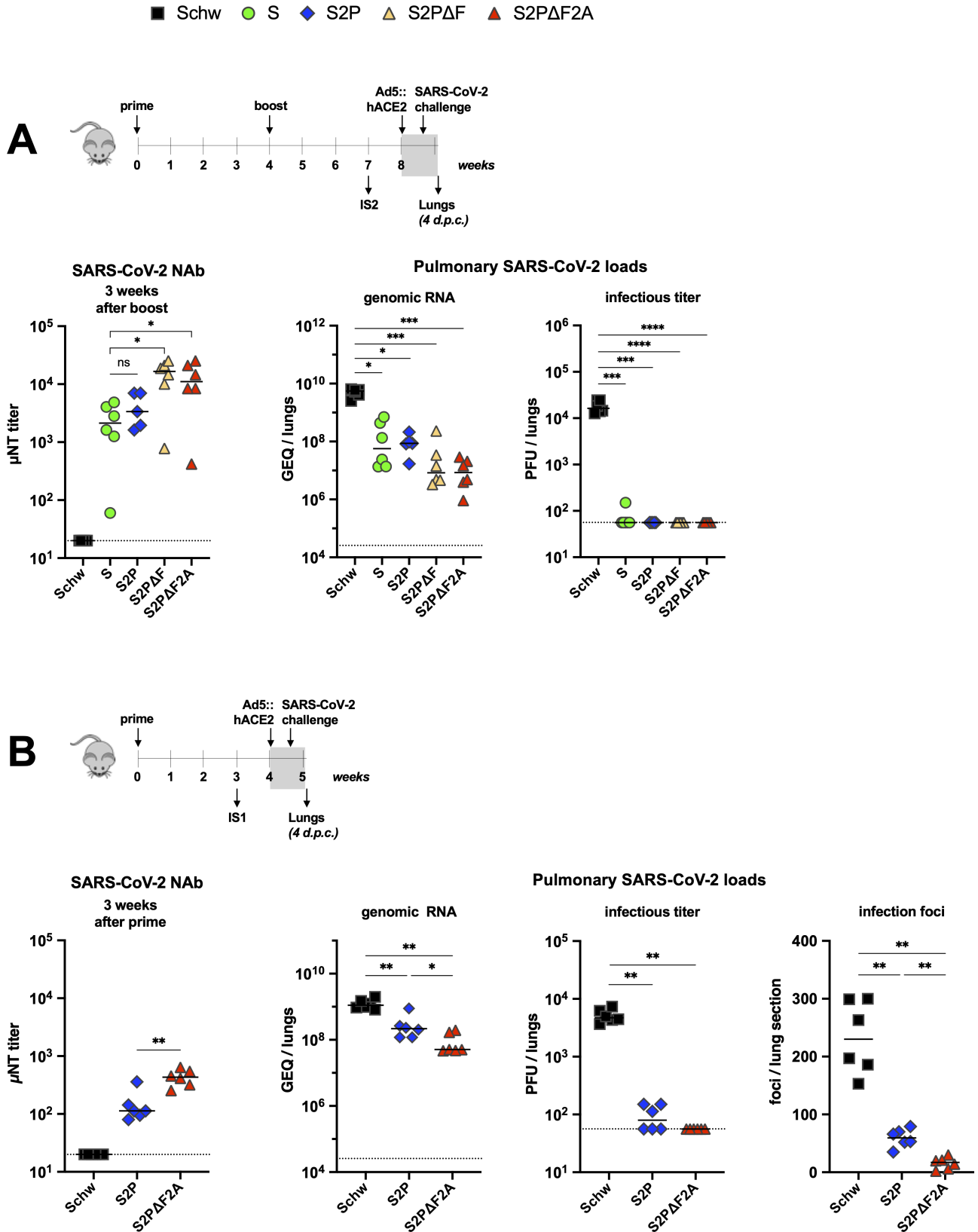


**FIG 6** Protection of mice against challenge with SARS-CoV-2 after prime/boost or single immunization. Schematic of the two experimental set-ups is shown. Mice ( $n = 5$  or  $6$  per group) were immunized twice with MV-ATU3-3 (S), MV-ATU3-S2P (S2P), MV-ATU3-S2PΔF (S2PΔF), MV-ATU3-S2PΔF2A (S2PΔF2A), or the parental MV Schwarz strain (Schw) (A) or once with MV-ATU3-S2P (S2P), MV-ATU3-S2PΔF2A (S2PΔF2A), or the parental Schw (B). SARS-CoV-2 microneutralization (Continued on next page)

**FIG 6** (Continued)

titers (NAb) in sera collected 3 weeks after boost (IS2, panel A) or 3 weeks after prime (IS1, panel B) were expressed as reciprocals of serum dilutions that resulted in inhibition of 95% of virus infectivity (left graphs). Following i.n. instillation with Ad5::hACE2 4 weeks after boost or prime and subsequent challenge with SARS-CoV-2, pulmonary viral loads were quantified 4 days after challenge as genomic RNA or infectious titer per lungs (middle graphs), and number of infection foci in IHC sections of the five lung lobes (right graph). Statistical significance was assessed using the non-parametric Kruskal-Wallis test with Dunn's uncorrected post hoc analysis (A) or Mann-Whitney test (B). ns: not significant, \* $P < 0.05$ , \*\* $P < 0.005$ , \*\*\* $P < 0.0005$ , \*\*\*\* $P < 0.0001$ .

0.005), in agreement with quantification of SARS-CoV-2 RNA levels and infectious titers (Fig. 6B).

Noticeably, whether after prime only or after prime-boost, neutralizing antibody titers in blood samples taken 4 days before the challenge inversely correlated with SARS-CoV-2 loads in the lungs of individual mice (regardless of the immunogen) as assessed by levels of GEQ RNA ( $r = -0.86$  and  $r = -0.82$ , respectively,  $P < 0.0001$  using Spearman non-parametric correlation coefficient analysis). This suggests that neutralizing antibody levels in the blood are important contributors to the reduction of SARS-CoV-2 replication after infection.

**Infection-driven bronchiolar lesions are reduced after single immunization**

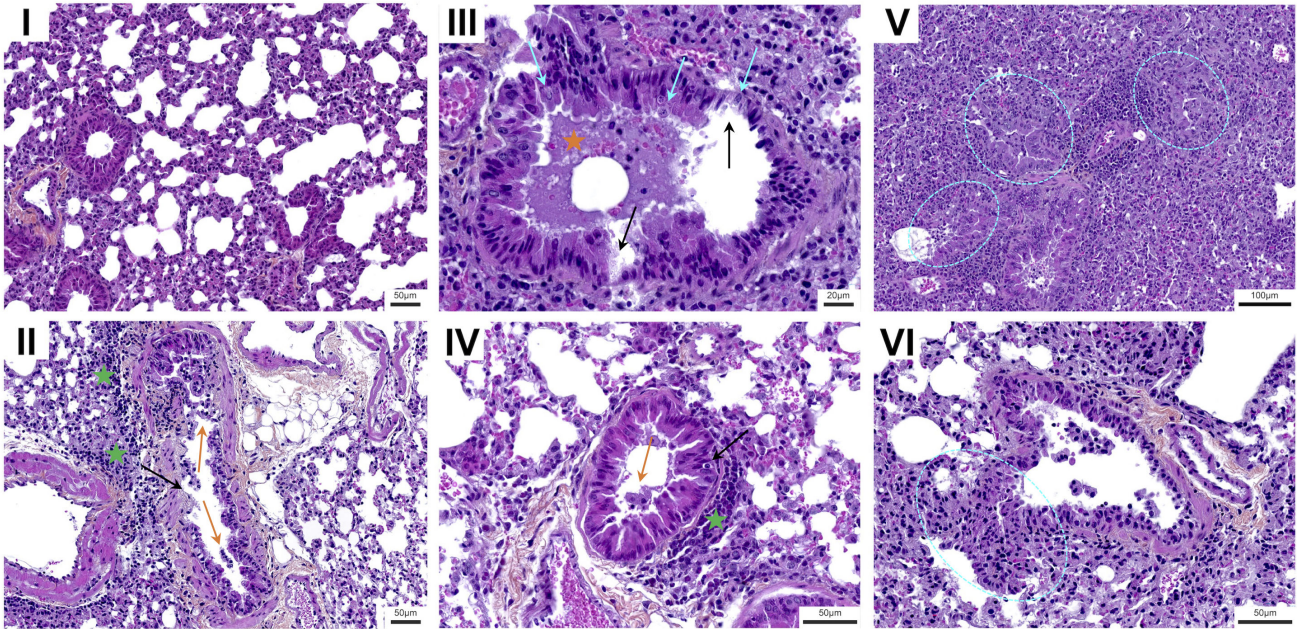
On lung histopathological examination of hematoxylin and eosin (H&E)-stained lung sections, treatment with Ad5::hACE2 alone (with no subsequent administration of live SARS-CoV-2) resulted in a mild-to-moderate widespread mononuclear interstitial infiltration of the lungs with minor alveolar involvement or disruption of the lung architecture, and hardly any perivascular or peribronchial infiltrates (Fig. 7A, panel I). Epithelial cell desquamation in the bronchiolar lumen was occasionally observed, and predegenerative lesions of the bronchiolar epithelial cells were rare.

Lung lesions in SARS-CoV-2-challenged mice, whether naïve controls or MVSchw-immunized mice, were overall severe, in spite of some inter-mouse and inter-lobe variation (Fig. 7A, panels II–VI). Lesions were characterized by a moderate-to-severe widespread interstitial syndrome, frequent bronchiolar damage, and multifocal desquamation of the respiratory epithelium (panels II–IV). Perivascular or peribronchial infiltrates (panel II), although more frequent than in Ad5::hACE2-treated mice, remained rare. Areas of parenchymal consolidation were observed that extended up to 80% of the lobe surface. These condensed areas were associated in various proportions with fading of the delineation between bronchioles and parenchyma (panels V and VI), disappearance of the alveoli (panel V), and dense mononuclear interstitial infiltration (panel VI), resulting in partial or complete disruption of the bronchiolar epithelium and organ collapse.

After SARS-CoV-2 challenge, MV-ATU3-S2P- and MV-ATU3-S2PΔF2A-immunized mice displayed lesions similar to in nature but less severe than those seen in control MVSchw-immunized mice. The widespread interstitial mononuclear infiltration, although occasionally severe, was largely reduced to mild-to-moderate grades. Due to elevated baseline of interstitial syndrome in Ad5::hACE2-treated mice and variations within groups of mice, this trend was, however, not statistically significant (Fig. 7B, left panel). Epithelial disruption, fading of the bronchiolar-parenchyma delineation, and predegenerative alterations of the bronchiolar epithelium were less frequent and less severe than in control mice. Semi-quantitative scoring of the bronchiolar lesions in H&E lung sections (Fig. 7B, right panel) demonstrated the statistical significance of this observation ( $P < 0.05$ ).

Histology data collectively indicate that immunization with a single administration of MV-ATU3-S2PΔF2A conferred substantial protection against SARS-CoV-2-induced lung pathology, without triggering a detrimental inflammatory response.

# A



# B

## Histopathologic scoring

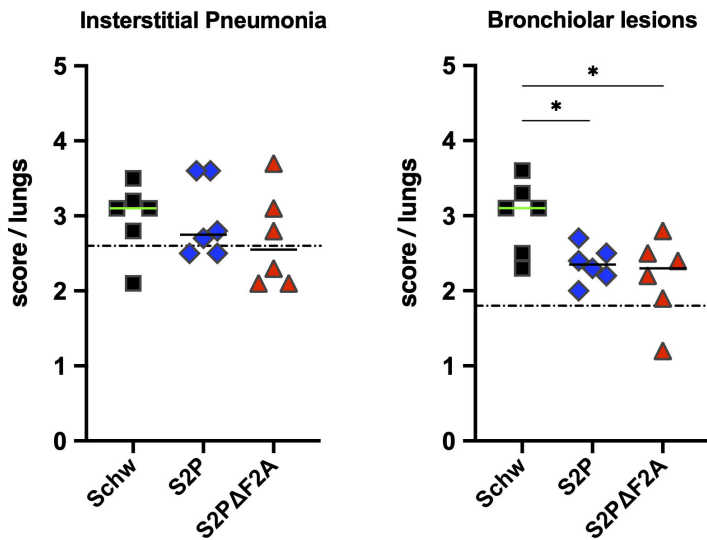


**FIG 7** Reduction of lung histopathology in challenged mice after single immunization. (A) Routine H&E staining of lung sections from control, non-vaccinated-mice which were instilled with Ad5::hACE2 and subsequently mock infected (I) or challenged with SARS-CoV-2 (II–VI). Green stars: marked infiltrate around the bronchiole and/or accompanying vessel. Orange stars or arrows: eosinophilic exudate and cells debris filling the bronchiole lumen. Black arrows: predegenerative or degenerative lesions of the bronchiolar epithelium. Blue arrows: intranuclear patches of condensed chromatin, suggestive of apoptosis, or signs of kariolysis. Blue circles: fading of bronchiole-parenchyma delineation. (B) Inflammation (interstitial pneumonia) and histopathological (bronchiolar) lesions from vaccinated and SARS-CoV-2-challenged mice taken from the cohorts described in Fig. 6B. Interstitial pneumonia and bronchiolar lesions were evaluated and scored on H&E sections of the five lung lobes according to a semi-quantitative zero-to-five severity rating, as described in the Materials and Methods. Green and black bars show medians. The dotted lines indicate median baselines of inflammation and bronchiolar lesions, respectively, in a group of three control, non-vaccinated mice, following i.n. instillation with Ad5::hACE2 only, in the absence of subsequent challenge with SARS-CoV-2. Statistical significance was assessed using the Mann-Whitney test. \* $P < 0.05$ .

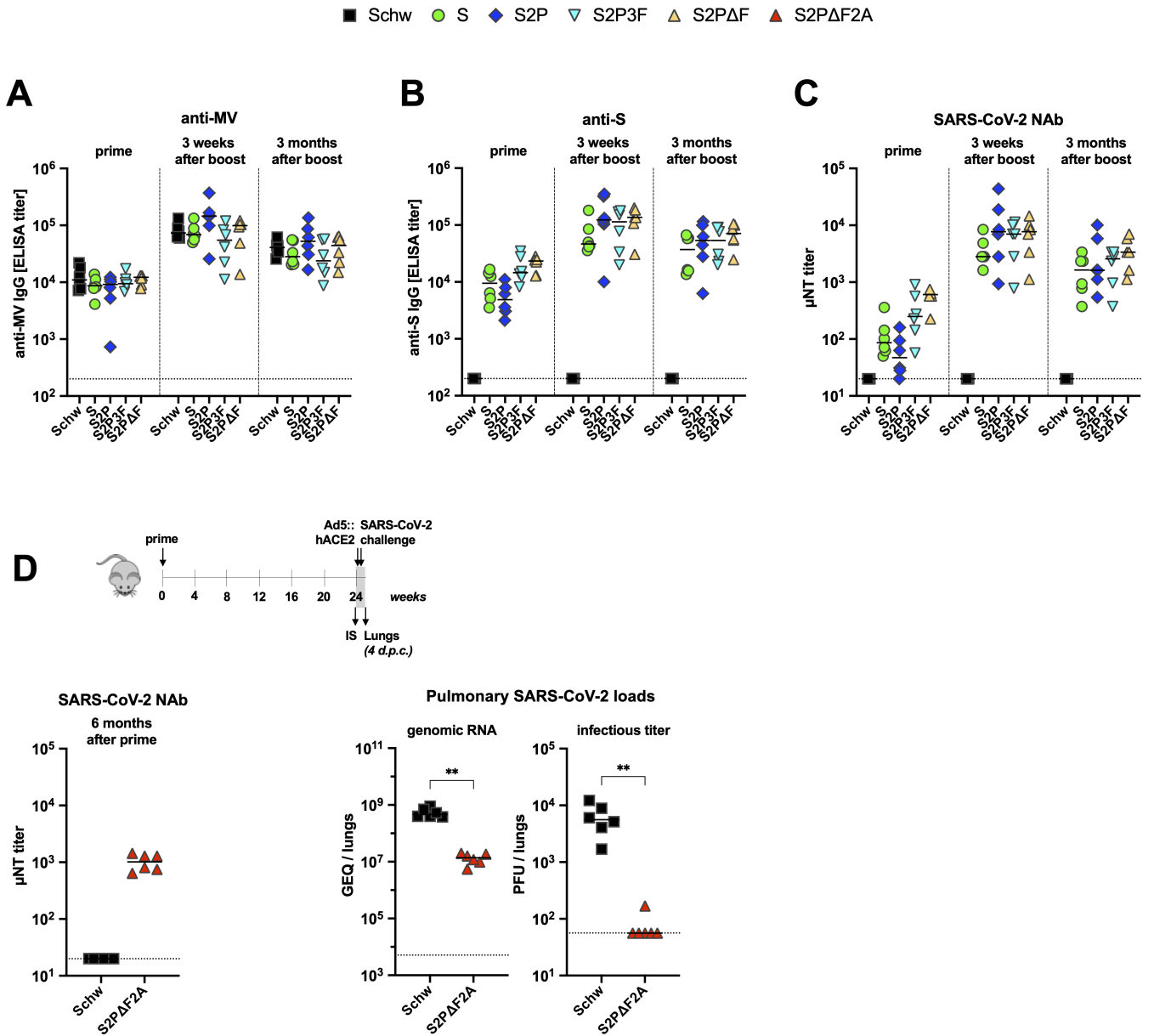


**FIG 8** Longevity of antibody response and protection after prime/boost or prime-only immunization. CD46-IFNAR mice ( $n = 6$  per group) were immunized twice with MV-ATU3-S (S), MV-ATU3-S2P (S2P), MV-ATU3-S2P3F (S2P3F), MV-ATU3-S2PΔF (S2PΔF), or the parental MV Schwarz strain (Schw) (A, B, C), and IFNAR-KO mice were immunized only once with parental Schw or MV-ATU3-S2PΔF2A (S2PΔF2A) (D). Antibody responses were measured in sera collected 3 weeks after prime, 3 weeks after boost, and 3 months after boost (A, B, C) or 6 months after prime (D) by measles-specific ELISA (anti-MV, panel A), SARS-CoV-2 spike-specific ELISA (anti-S, panel B), or microneutralization assay (NAb, panels C, D). The mice were instilled with Ad5::hACE2 and challenged with SARS-CoV-2 6 months after single immunization as described in the schematic (D). Pulmonary SARS-CoV-2 loads were quantified 4 days after challenge as genomic RNA (left graph) and infectious titer (right graph) per lungs. Statistical significance was assessed using the Mann-Whitney test. \* $P < 0.05$ , \*\* $P < 0.005$ .

### Antibody responses are long lived and protect up to 6 months after single immunization

To determine whether one or two immunizations were able to induce long-lived SARS-CoV-2 neutralizing antibodies, groups of mice were immunized with two injections of  $1 \times 10^5$  TCID<sub>50</sub> of MV-ATU3-S, -S2P, -S2P3F, or -S2PΔF at a 4-week interval (Fig. 8A through C) or with a single injection of MV-ATU3-S2PΔF2A (Fig. 8D, left panel). In the two-dose experiment, antibodies were monitored 3 weeks after prime, as well as 3 weeks and 3 months after boost, respectively. As shown in Fig. 8B, all MV recombinant

viruses tested induced anti-spike antibodies in the  $10^4$  ELISA-unit range after prime and in the  $10^5$  ELISA-unit range after boost. The same hierarchy in the magnitude of the antibody responses was observed as in previous experiments shown in Fig. 4, i.e., MV-ATU3-S2P3F and -S2PΔF induced higher levels of S-specific and SARS-CoV-2 neutralizing antibodies after prime than MV-ATU3-S and -S2P (Fig. 8B and C). Most importantly, S-specific and SARS-CoV-2 neutralizing antibody titers remained high when measured 3 months after boost. Of note, ELISA and neutralizing antibody titers shown in Fig. 8B and C, obtained in CD46-IFNAR mice, were very similar to those reported in Fig. 4B, C, E, and F obtained in IFNAR-KO mice, confirming that the presence of human CD46 does not significantly improve measles vector replication in the IFNAR-KO model, as reported (46). In the single immunization experiment with MV-ATU3-S2PΔF2A, sustained, long-lived SARS-CoV-2 neutralizing antibody titers were measured in the  $10^3$  microneutralization-unit range approximately 6 months after prime (Fig. 8D, left panel). Accordingly, long-term protection against SARS-CoV-2 challenge in the Ad5::hACE2 model after a single immunization proved highly efficacious and translated to notably reduced GEQ RNA levels and absence of infectious particles in the lungs of most mice (Fig. 8D, right panels), with similar magnitude of reduction as shortly after the prime (Fig. 6B).

## DISCUSSION

In this study, we generated and evaluated a series of measles-vectored COVID-19 vaccine candidates expressing the native or modified SARS-CoV-2 spike protein and selected a candidate by June 2020 that was moved into clinical development in August 2020, 7 months after the release of the SARS-CoV-2 Wuhan sequence. Based on the pandemic context, our aim was to develop a candidate that was highly efficacious, ideally after a single immunization. At that time, no measles vector-based SARS-CoV-2 vaccine approach was yet published. We found that recombinant MVs expressing a prefusion-stabilized, full-length spike protein with deleted furin cleavage site (MV-ATU3-S2PΔF and MV-ATU3-S2PΔF2A) were the most immunogenic, elicited the highest levels of SARS-CoV-2 neutralizing antibodies, induced robust Th1-oriented T cell responses, and proved highly protective against challenge with an early pandemic isolate of SARS-CoV-2 in IFNAR-KO mice. These results supported moving one of these MV-based candidates into further development. As discussed below, we selected MV-ATU3-S2PΔF2A (clone V591, onward referred to as MV-ATU3-S2PΔF2A/V591), which was shown to be also protective in non-human primates (see companion article by Nambulli et al. [37]). The clinical trials with MV-ATU3-S2PΔF2A/V591 were conducted between August 2020 and May 2021 ([ClinicalTrials.gov](https://clinicaltrials.gov/ct2/show/study/NCT04497298), [NCT04497298](https://clinicaltrials.gov/ct2/show/study/NCT04498247) and [NCT04498247](https://clinicaltrials.gov/ct2/show/study/NCT04498247)). Unexpectedly with respect to its high efficacy in the two preclinical models, the candidate was found to elicit insufficient immunogenicity in humans (38, 39).

Based on our experience with SARS-CoV (26), a recombinant measles vector expressing the full-length, membrane-anchored native form of the spike protein was our original lead candidate. Recombinant MVs harboring a codon-optimized S sequence in ATU2 were genetically unstable or produced low-titered viral stocks (Fig. 1B). Such an impaired growth has also been described by Hörner et al. using a different MV backbone and optimized S sequence inserted at a similar position (58). We hypothesized that it was probably due to too high expression of the spike protein when the codon-optimized heterologous sequence was inserted between the MV P and M genes (ATU2, position 3 of MV antigenome) as compared to between the H and L genes (ATU3, position 6), consistent with the gradient of gene expression generated by MV genome transcription (59).

In contrast, recombinant MV expressing the fully codon-optimized native S sequence from ATU3 grew at MV-like rates (Fig. 3B). However, such candidate exhibited a hyperfusogenic phenotype (Fig. 1D and Fig. 3A), as also observed by Hörner et al. (58) and with a recombinant adenovirus 26 vector (60) and was thus deprioritized for further development.

The introduction of the two stabilizing proline residues (2P) in the hinge loop at the C-terminus of heptad repeat 1 of the S2 subunit (MV-ATU3-S2P) abolished the enhanced fusogenic phenotype (Fig. 2B and Fig. 3A), in-line with the inhibition of S-driven cell-cell fusion that we observed in the transient cell fusion assay (Fig. 2B) and the locking of the spike in its prefusion form reported by Wrapp et al. (14). Similar observations were reported as part of the development of the Ad26-based vaccine from Janssen/Johnson & Johnson (60). The benefit of the introduction of proline residues for reducing the fusogenic activity of viral glycoproteins was first described for influenza virus hemagglutinin (61) and HIV envelope protein (62), and found to further hold true for RSV fusion protein (63), MERS-CoV spike (42), and SARS-CoV spike (43), pointing to a universal strategy for improving viral surface protein stability in vaccine design.

Furthermore, such prefusion-stabilizing proline residues were shown to enhance humoral immune responses in preclinical development of vaccine candidates against RSV (41, 64) and MERS-CoV (42). Accordingly, BioNTech/Pfizer BNT162b2 and Moderna mRNA-1273 SARS-CoV-2 mRNA vaccines (51, 65) were developed with prefusion-stabilized spike containing the 2P mutation. In our study, the humoral immune responses were not significantly improved by the 2P mutation (MV-ATU3-S2P, Fig. 4B and C). This is consistent with data from Liu et al. who reported no improvement of the S-2P immunogen over the native S in the MVA-based vector (66), while in other technologies, e.g., the gorilla adenoviral vector, an increase of immunogenicity was observed (67).

Importantly, in our study, neutralizing responses were markedly increased using candidates expressing prefusion-stabilized spike together with inactivated furin cleavage site (S2P3F, S2PΔF, S2PΔF2A), particularly after a single immunization, and with a trend for better performance of the deletion over the mutation of the cleavage site (Fig. 4B, C, E, and F). The furin S1/S2 cleavage is a unique feature to SARS-CoV-2 that distinguishes it from the related SARS-CoV (13, 14). Although an active S1/S2 cleavage site is required for S-mediated SARS-CoV-2 entry into human lung cells (16), or more generally for entry into TMPRSS2-expressing cells that are typically abundant in respiratory tissue (20), abrogating S1/S2 cleavage did not impact virus entry into VeroE6 cells lacking TMPRSS2 (13, 16, 20). This indicates that altering the multibasic S1/S2 cleavage site may stabilize the spike without causing extensive structural alteration, supporting enhanced spike immunogenicity in consistence with the prevention of S1 shedding (13). Similarly to our findings, a noncleavable form of SARS-CoV-2 S was found to elicit overall higher neutralizing antibody titers in hamsters than the native counterpart expressed from yellow fever virus 17D vaccine vector (68), and a noncleavable prefusion-stabilized S induced more robust neutralizing antibody responses and protection against challenge than native S after single delivery with an Ad26 vector in rhesus macaques (69). In an approach with a different measles vector described by Lu et al. (70), MV expressing a prefusion-stabilized form of soluble S carrying a deletion of the furin cleavage site was more immunogenic than MV expressing full-length native S, in accordance with our data.

While in the preclinical IFNAR-KO mice model, we did not observe any added value of the 2A mutation engineered to inactivate spike ERRS in MV-ATU3-S2PΔF2A compared to MV-ATU3-S2PΔF (Fig. 4D through F and Fig. 5), MV-ATU3-S2PΔF2A/V591 was prioritized in June 2020 for further development based on the theoretical benefit the inactivation of the ERRS might offer in another host. We hypothesized that ERRS inactivation could positively impact S immunogenicity not only by a small increase in its cell surface expression [initially known for SARS-CoV (45) and reported recently for SARS-CoV-2 (71)] but also by preventing its retrograde Golgi to ER transport, possibly resulting in its ER accumulation and induction of detrimental ER stress (72). A combination of 2P prefusion-stabilizing mutation, furin site inactivation, and deletion of the ERRS has also been described within a series of MVA-based SARS-CoV-2 vaccine candidates (66), but no benefit of the ERRS mutation to immunogenicity and protection was identified either.

Importantly, a single immunization with MV-ATU3-S2PΔF2A/V591 was sufficient to elicit levels of SARS-CoV-2 neutralizing antibodies in IFNAR-KO mice that were comparable to those present in a high-titer COVID-19 convalescent patient reference

serum (20/130 NIBSC research reagent). A boost immunization increased neutralization antibody levels by about 10-fold for all candidates (Fig. 4B, C, E, and F) and, for MV-ATU3-S2PΔF2A/V591, to levels about 100-fold higher than those in human convalescent serum (Fig. 4G).

MV-ATU3-S2PΔF2A/V591 also performed best in terms of protection against SARS-CoV-2 challenge in a mouse model that transiently expresses hACE2 via adenovirus transduction. Control of viral replication in the lungs (Fig. 6B) was demonstrated after single immunization, as attested by lower SARS-CoV-2 genomic RNA loads and undetectable infectious particles, as well as very few infection foci, if at all. Reduced pulmonary pathology could also be demonstrated after single vaccine administration, with bronchiolar lesions (Fig. 7B, right panel) as in mice treated with Ad5:hACE2 only (without SARS-CoV-2 instillation). It should be noted that the latter treatment triggered moderate baselines of interstitial syndrome and bronchiolar lesions in this study that were higher than previously reported in a collaborative study (54) or by others (57), although similar doses of Ad5 vectors were administered. This may be due to absence of IFN signaling in the IFNAR-KO mice used in our study or to their different genetic background (129/Sv). In this model, median inflammation levels recorded in MV-ATU3-S2PΔF2A/V591-immunized and -challenged mice were similar to those observed in non-vaccinated/non-challenged mice (Fig. 7B, left panel), and no sign of enhanced pathology associated with eosinophilic infiltration or severe inflammation of the lungs was observed.

This mouse model paved the way to demonstrating immune-mediated control by Measles vector vaccination of SARS-CoV-2 replication and some aspects of SARS-CoV-2 lung pathology *in vivo*. In the companion article by Nambulli et al. (37), we confirmed that MV-ATU3-S2PΔF2A/V591 was efficacious in an established African green monkey model of disease. V591-vaccinated animals developed potent neutralizing antibodies as well as S-specific T cells and demonstrated reduced viral loads after challenge. Most interestingly, using a combination of non-invasive PET-CT imaging in living animals and histologic investigation at necropsy, we demonstrated that their respiratory tract was protected from disease burden.

Another important point during the development of our SARS-CoV-2 vaccine was to demonstrate the induction of a Th1-skewed T cell immune response in the preclinical models to minimize the theoretical risk of vaccine-associated enhanced respiratory disease (VAERD). VAERD was first observed with the F-RSV vaccine (73) and in animal model studies with SARS-CoV vaccine candidates (49, 74) but was not seen with vaccine candidates and formulations known to generate a Th1-type response through the use of either Th1-driving adjuvants or viral vectors (75, 76). At the beginning of the COVID-19 pandemic, it was unclear if VAERD would be a relevant concern for SARS-CoV-2 vaccines for humans. Nevertheless, the induction of a Th1-type skewed immune response was considered a safety measure and recommended by ICMRA (48). Later, several groups indeed confirmed that vaccination regimens inducing weak neutralizing antibody levels and Th2-shifted immune responses enhanced respiratory disease with eosinophilic immunopathology and proinflammatory cytokines after SARS-CoV-2 challenge both in mouse (77, 78) and hamster models (79), highlighting that the early recommendation for Th1-driving vaccines was correct and important. Our experimental data confirmed that a Th1-biased immunity was induced by all MV-SARS-CoV-2 vaccine candidates, as was previously shown for our MV-SARS-CoV (26), an MV-based vaccine against Lassa fever (26, 80) and the standard measles vaccine (81). A strong CD8<sup>+</sup> population and a slightly less frequent CD4<sup>+</sup> T cell population producing Th1 cytokines (TNF-α and IFN-γ) were detected in splenocytes of immunized mice upon stimulation with S peptide pools (Fig. 5A and C), whereas no CD4<sup>+</sup> T cells producing Th2 cytokines IL-5 and IL-13 were detected (Fig. 5B). The level of Th1 over Th2 involvement with our MV-SARS-CoV-2 vaccine candidates was in-line with, if not better than, Moderna and BioNTech mRNA vaccines (51, 65) and adenoviral vector-based SARS-CoV-2 vaccines (60, 82).

Finally, an important feature of a viral-vectored vaccine in the context of the pandemic is a high growth rate for a high yielding manufacturing process and the possibility to largely expand the original seeds for the production of the billion doses required globally to reach herd immunity (83). The robust, MV-like growth rate (Fig. 3B) and genetic stability over serial passages of MV-ATU3-S2PΔF2A/V591, together with the strong preclinical data as discussed above and the prior promising clinical experience with the MV-CHIK vaccine (34, 36, 84), fully warranted the initiation of phase I/II clinical trials in August 2020 ([ClinicalTrials.gov](https://clinicaltrials.gov/ct2/show/study/NCT04497298), [NCT04497298](https://clinicaltrials.gov/ct2/show/study/NCT04498247), [NCT04498247](https://clinicaltrials.gov/ct2/show/study/NCT04498247)).

The results of these clinical trials (38, 39) revealed that MV-ATU3-S2PΔF2A/V591 was safe and well tolerated in humans. However, despite the strong and protective immunogenicity of MV-ATU3-S2PΔF2A/V591 in the mouse model as described here, as well as in an NHP model (see companion article by Nambulli et al. [37]), the immunogenicity in humans was low. Two injections of the high dose ( $10^6$  TCID<sub>50</sub>) in the Institut Pasteur-sponsored study (NCT04497298) elicited spike-binding IgG antibodies in 78% and SARS-CoV-2 neutralizing antibodies in 61% of participants 1 month after the second injection. In the MSD-sponsored study (NCT0449824), spike binding and SARS-CoV-2 neutralizing antibodies after a single V591 administration were only observed in participants who received the highest tested dose ( $10^7$  TCID<sub>50</sub>), and the antibody responses were generally lower than those observed in a panel of sera obtained from patients who had recovered from COVID-19 (38). Therefore, the immunogenicity of V591 in humans was considered insufficient to support further development. In contrast, the MV-CHIK vaccine candidate administered at a comparable dose in phase I and II trials induced neutralizing antibodies in >85% of participants after single administration and >95% of participants after two injections (34, 36). Very recently, Tschismarov et al. reported results of a phase I clinical study of a recombinant measles Schwarz-vectored Lassa fever vaccine candidate (MV-LASV) (85). Two injections induced LASV-specific IgG in 100% of participants receiving  $10^5$  TCID<sub>50</sub>, while a single immunization did not result in detectable LASV-specific IgG. No neutralizing antibodies were induced in either treatment group. At the same dose ( $10^5$  TCID<sub>50</sub>), V591 elicited SARS-CoV-2-specific IgG in 67% vaccine recipients after two injections and in 13% after single immunization (39), indicating moderate humoral immunogenicity of MV-LASV in-between MV-CHIK and V591.

Surprisingly, pre-existing anti-measles immunity showed a statistically significant impact on the response to V591 in the phase I trial (39), whereas immunogenicity of the MV-CHIK candidate vaccine was not affected in the phase I and II trials (34, 36). For MV-LASV also, no impact of pre-existing anti-measles immunity was observed across all vaccinees; however, the analysis may be confounded by an inadvertent bias in the anti-MV Ab levels at baseline between the high- and low-dose groups (85). While an impact of pre-existing anti-vector immunity is not uncommon for viral-vectored vaccines (86) and has been observed, for instance, with an adenovirus-vectored COVID-19 vaccine (87), the difference in sensitivity to pre-existing MV immunity between the MV-based candidates is striking. One notable difference between the candidates is that MV-CHIK generates CHIKV virus-like particles (VLPs) (88). If already present in the vaccine preparation, VLPs may contribute to the immunogenicity of this candidate, rendering the overall response less dependent on the rate of *de novo* antigen production in vaccinated individuals and the MV-CHIK candidate advantageously resilient to pre-existing anti-MV immunity. Other differences relate to antigen designs, as already discussed in Launay et al. (39), i.e., the prefusion-stabilized and functionally inactivated spike protein used in V591 compared to native viral glycoproteins in other clinical candidates. However, we feel unlikely this may be the cause of low clinical immunogenicity since the preclinical results reported here show a major improvement of immunogenicity for the 2PΔF-modified antigen compared to the native S, and the same has been observed for the Ad26-vectored vaccine from Janssen/Johnson & Johnson (60). Investigational studies are ongoing to understand the underlying mechanistic reasons for the limited immunogenicity of V591 in humans, particularly in regard of the strong protective data

in the two murine and NHP preclinical models. It will be very important for the measles vector community to understand the factors underlying the resistance or sensitivity of the different candidates to pre-existing anti-measles immunity for future developments of the platform technology.

## MATERIALS AND METHODS

### Cells and viruses

FRhK-4 cells (Fetal Rhesus monkey Kidney) and Vero-NK cells (African Green Monkey Kidney cells, clonally derived from the Vero E6 cell line) (89) were cultured at 37°C under 5% CO<sub>2</sub> in Dulbecco's modified Eagle medium containing 4.5 mg/mL L-glucose, 100 U/mL penicillin, and 100 µg/mL streptomycin (complete DMEM), supplemented with 5% heat-inactivated fetal bovine serum (FBS) (DMEM-5). Helper 293-T7-NP cells stably expressing T7 RNA polymerase and N and P genes from the vaccine Measles Schwarz strain were grown in complete DMEM supplemented with 10% FBS (DMEM-10). The Measles Schwarz vaccine strain was rescued and amplified in the laboratory as previously described (26).

The BetaCoV/France/IDF0372/2020 strain of SARS-CoV-2 was isolated by the National Reference Center (NRC) for Respiratory Viruses (S. van der Werf) hosted by Institut Pasteur (Paris, France), as already described (90). The oropharyngeal swab from which this strain was isolated was sampled in January 2020 from a paucisymptomatic woman in Paris, France and has been provided by X. Lescure and Y. Yazdanpanah from Bichat Hospital (Paris, France). The virus was kindly supplied after a single additional passage (P2) in Vero E6 cells from the initial isolation. In order to obtain large-volume working stocks, we further amplified the virus at 37°C by a single passage (P3) in Vero-NK cell monolayers at a multiplicity of infection of 10<sup>-4</sup> in complete DMEM containing 10 mM Tricine pH 7.4 and 1 mg/mL BSA (DTB), supplemented with 0.5 µg/mL TPCK-treated trypsin. The infectious titers of the viral stocks used for mouse challenge experiments and microneutralization assays were determined by PFU assay in Vero-NK cells (see below) and by standard limiting dilution assay in FRhK-4 cell monolayers in 96-well microtiter plates (40), respectively.

Whole-genome sequencing of the original sample and of the P2 and P3 passages was performed by RNA-Seq at the NRC by Illumina NextSeq 500 next-generation sequencing and deposited after assembly on the GISAID EpiCoV platform under accession numbers EPI\_ISL\_406596, EPI\_ISL\_410720, and EPI\_ISL\_18072209. It revealed only two clonal mutations when compared to the early outbreak SARS-CoV-2 reference strains Wuhan-Hu-1 (Genbank: MN908947) and hCoV-19/Wuhan/WIV04/2019 (GISAID: EPI\_ISL\_402124) isolated in Wuhan in December 2019: G22661T (S-V367F) and G26144T (NS3-G251V). Notably, an average NGS coverage at more than 50,000× of the P3 virus genome revealed no single-nucleotide polymorphism (SNP), deletion, or insertion at or around the S1/S2 cleavage site of the spike protein with a detection limit of less than 2% (see raw data associated with EPI\_ISL\_18072209).

The Ad5::hACE2 viral stocks were produced using ViralPower Adenoviral Promoterless Gateway Expression Kit (Thermo Fisher), purified, and titrated using a real-time quantitative PCR assay, as described in Ku et al. (54).

### Antibodies

Anti-SARS-CoV S polyclonal mouse and rabbit antibodies have been described previously (40). We demonstrated that these antibodies cross-reacted with the S protein expressed in SARS-CoV-2-infected VeroE6 cells. Anti-SARS-CoV-2 S polyclonal antibodies were also raised in rabbits against recombinant trimerized SARS-CoV-2 spike ectodomain expressed and purified from Expi 293F cells transfected with plasmid pCI-S2P3F-T4-8HIS (see ELISA section).

Anti-MV nucleoprotein polyclonal rabbit antibodies were purchased from Covalab (#pab0035). AlexaFluor-488 and -680-conjugated anti-rabbit or anti-mouse IgG antibodies

were purchased from Invitrogen (# A21202, # A21206, # A10043, # A10038). Anti-mouse IgG secondary antibody (gamma-specific), or isotype-specific anti-IgG1 or anti-IgG2a secondary antibodies coupled to horseradish peroxidase were purchased from Southern Biotech (# 1030–05, # 1070–05, # 1080–05).

## Plasmids

A synthetic gene encoding spike (S) protein from the Wuhan-Hu-1 isolate of SARS-CoV-2 was designed based on the Genbank MN908947 sequence. Spike coding sequence was optimized at the transcriptional, mRNA, and translational levels for high expression in mammalian cells through the Project Manager platform of GeneArt (ThermoFisher). Typically, in addition to codon usage bias optimization for human cells, regions of very high (>80%) or low (<30%) GC content were avoided, whenever possible, and *cis*-acting sequence motifs like internal TATA-boxes, *chi*-sites, ribosomal entry sites, ARE, INS, and CRS sequence elements, as well as repetitive sequences, RNA secondary structures, splice donor and acceptor sites, and branch points were avoided. The sequence was further edited to remove MV editing (AnGm,  $n + m = 6$  and  $n \geq 3$ )- and core gene end (A4CKT)-like sequences on both strands. *Bsi*WI and *Bss*HII restriction sites were added at the 5' and 3' ends of the gene sequence, respectively.

This codon-optimized S sequence was subcloned into the pCI mammalian expression vector (Promega), resulting in plasmid pCI-S. Lysine and valine codons at positions 986 and 987 of S, respectively, were further substituted for proline codons (K986P and V987P, referred to as "2P" mutation) by overlapping PCR amplification (91) using the synthetic gene as template and oligonucleotides 2P\_for1/2P\_rev1 and 2P\_for2/2P\_rev2 depicted in Table S1. Mutated PCR fragments were assembled into pCI using the restriction-free, In-Fusion cloning system (Takara). Similarly, arginine codons of the FCS at positions 682, 683, and 685 of S were substituted by glycine or serine codons (R682G, R683S, and R685G, respectively, referred to as the "3F" mutation) using oligonucleotides 3F\_for1/3F\_rev1 and 3F\_for2/uni\_rev indicated in Table S1. Oligonucleotides  $\Delta F$ \_for1 /  $\Delta F$ \_rev1 and  $\Delta F$ \_for2/uni\_rev (Table S1) were used to introduce a deletion of the 11-amino acid loop (Q675-R685) encompassing the FCS (referred to as " $\Delta F$ "). The sequence of all constructs' inserts was verified by Sanger sequencing of respective plasmid clones (Eurofins).

MV Schw-derived plasmids were produced as follows. First, pKM2-eGFP was obtained by transferring the whole T7 rescue cassette (17,038 bp located between the two *Not*I sites) of the original pTM-MV Schw-ATU2 (pTM2-eGFP) plasmid (33) into a purposely modified version of the commercial pENTR2 minimal plasmid (ThermoFisher). Plasmids pKM2-eGFP and pTM2-eGFP carry identical infectious cDNAs corresponding to the anti-genome of MV Schw and an additional transcription unit between the P and M genes (ATU2) encoding the eGFP protein. They contain unique *Bsi*WI and *Bss*HII restriction sites for substitution of the eGFP-coding sequence by foreign open reading frames. In the pKM2-eGFP plasmid, the T7 promoter of the rescue cassette is preceded by a unique *Asi*S1 site, and the T7 terminator is followed by a unique *Not*I site. Next, pKM3-eGFP was derived from pKM2-eGFP by substituting the *Sbf*I-*Not*I fragment of pKM2-eGFP by the corresponding fragment of pTM-MV Schw-ATU3 (33). The pKM3-eGFP vector thus carries an infectious MV Schw cDNA with an additional transcription unit between the H and L genes (ATU3) encoding the eGFP protein. The codon-optimized S sequence was cloned into both pKM2-eGFP and pKM3-eGFP between *Bsi*WI and *Bss*HII restriction sites to generate pKM-ATU2-S and pKM-ATU3-S, respectively. The resulting cDNAs respect the "rule of six," which stipulates that the number of nucleotides of the MV genome must be a multiple of 6 (92, 93).

Derivatives of pKM-ATU3-S containing 2P, 2P3F, or 2P $\Delta F$  substitutions were engineered by cloning mutated S sequences from the corresponding pCI-S plasmids into pKM-ATU3-eGFP between *Bsi*WI and *Bss*HII restriction sites, yielding plasmids pKM-ATU3-S2P, -S2P3F, or -S2P $\Delta F$ , respectively. Prior to insertion of S2P $\Delta F$ -coding sequence into pKM-ATU3, a second PCR was performed on pCI-S-2P $\Delta F$  to respect the rule of six in the

MV vector using oligonucleotides uni\_for/ $\Delta$ F\_rev3 (Table S1). The substitution of codons at positions 1269 and 1271 of S2P $\Delta$ F toward alanine codons (K1269A and H1271A, respectively, referred to as “2A” mutation) was directly engineered into pKM-ATU3 by PCR-based mutagenesis on pCI-S2P $\Delta$ F using oligonucleotides uni\_for/2A\_rev (Table S1).

To produce the mammalian expression plasmid pCI-S2P3F-T4-strep, a codon-optimized nucleotide fragment encoding the signal peptide and ectodomain of the uncleaved prefusion form of SARS-CoV-2 spike protein (S2P3F, amino acids 1–1211) was amplified by PCR from the synthetic gene described above, fused to a codon-optimized synthetic fragment encoding the trimerization foldon domain of bacteriophage T4 fibrin (referred to as “T4”) and a Twin Strep-tag (IBA Life Science, referred to as “strep”), and subcloned into pCI. The T4 fibrin foldon (g<sup>1</sup>yipeaprdgqA<sup>12</sup>YVRKDGWVLL<sup>23</sup>stfl) is used here as an artificial trimerization domain ( $\beta$ -hairpin propeller) for mimicking spike trimeric assembly at the virion surface (94). The pCI-S2P3F-T4-8HIS plasmid encodes a trimerized spike construct with a carboxy-terminal polyhistidine tag instead of a Twin Strep-tag. To produce the insect expression plasmid pMT-BiP-S2P3F-T4-strep, a nucleotide fragment encoding the S2P3F-T4-strep polypeptide without the native spike signal peptide was amplified by PCR from pCI-S2P3F-T4-strep and subcloned into the pMT/BiP/V5-His expression vector (Invitrogen). This construct thus has a *Drosophila* BiP signal sequence fused at the amino-terminal end of the spike ectodomain for efficient translocation into the ER of the transfected S2 insect cells.

Plasmids used in the GFP-split fusion assay were obtained from Addgene: TMPRSS2 was a gift from Roger Reeves (Addgene plasmid # 53887); pcDNA3.1-hACE2 was a gift from Hyeryun Choe (Addgene plasmid # 1786).

### Rescue and amplification of recombinant MVSchw-S viruses

The pKM-ATU2-S, pKM-ATU3-S, and derivative cDNAs encoding S mutants (see Plasmids section) were used to rescue recombinant measles viruses in a helper-cell-based system essentially as previously described (26).

Specifically, to yield recombinant MV-ATU2-S, MV-ATU3-S, and S derivatives, HEK 293-T7-NP cells at 50%–70% confluency in 6-well plates were co-transfected with each corresponding pKM-ATU2/3 S plasmid and the pEMC-La plasmid encoding MSchw polymerase using calcium phosphate. After an overnight incubation at 37°C in 5% CO<sub>2</sub>, cells were submitted to a 3-h heat shock at 43.5°C in 5% CO<sub>2</sub> and further incubated at 37°C for another 48 h. Transfected cells were then resuspended in their culture medium and co-cultured with Vero-NK cells seeded in 48-well plates. From day 3 of co-culture, cells were harvested from wells harboring single foci of cytopathic effect (CPE) or syncytia by trypsination, transferred into 6-well plates, and incubated at 37°C in DMEM-5. When syncytia/CPE reached 30%–50% of the cell monolayer, the rescued viral clones were further expanded in 75 cm<sup>2</sup> flasks. When syncytia CPE reached 70%–90% of the cell monolayer, cells were scraped in 1.5 mL of culture medium and lysed by one freeze/thaw cycle. Clarified lysates following a 5-min centrifugation at 2,000 g at 4°C were designated as passage 0 (P0) stocks, aliquoted, and stored at –80°C. Infectious titers were determined by endpoint limiting dilution assay in Vero-NK cells as geometric means of at least four independently measured titers.

Recombinant viruses were further amplified in Vero-NK cells in 150 cm<sup>2</sup> flasks infected at an MOI of 0.05 and cultured in DMEM-5. At 2–3 days post-infection, when syncytia/CPE reached 80%–95% of the cell monolayer, virus was harvested by one freeze/thaw cycle of the cells in 2.5 mL of culture medium, yielding passage 1 (P1) viral stocks. Similarly, recombinant viruses were serially passaged in cells for up to five additional passages.

Recombinant virus stocks were used to infect Vero-NK cells at an MOI of 0.05 in 6-well plates, and neosynthesized cell-associated virus was harvested at various time points p.i. by one freeze/thaw cycle of the cell monolayers scraped in 0.5 mL of complete DMEM. Clarified lysates were titrated by endpoint limiting dilution assay to establish viral growth curves.

## Viral genome sequencing

Recombinant MV genomic RNAs were extracted from P0 or P1 viral stocks using QIAamp Viral RNA Mini Kit (Qiagen). RNA was subjected to one-step reverse transcription and PCR using Superscript IV One-Step RT-PCR system (Invitrogen) and primers flanking the ATU2 (MV/+3224 and MV/-/3659) or the ATU3 (MV /+/8809 and MV/-/9540). The resulting PCR products were subjected to Sanger sequencing (Eurofins) of both DNA strands using a set of primers spanning the S sequence and upstream/downstream intergenic MV sequences.

For next-generation sequencing (NGS) analysis, genomic RNAs were extracted from P1 or P5 viral stocks and subjected to reverse transcription using the Transcriptor High Fidelity cDNA Synthesis Kit (Roche) and random hexamers. Resulting cDNAs were subjected to PCR amplification using the high-fidelity Phusion Hot Start II polymerase (Invitrogen) and a set of six or seven primer pairs designed to generate 4–6 kb DNA fragments overlapping by ~0.5 kb, spanning the entire MV genome (primer sequences available upon request). Overlapping PCR products were then mixed in an equimolar ratio and used to generate Illumina TruSeq PCR-free libraries following fragmentation into 550-bp-long fragments and UDI indexation (Illumina). Paired-end sequencing was performed on a MiSeq system with a nano v2 flowcell and reagents for 500 cycles (Illumina).

Quasi-species were analyzed using the variant calling pipeline from the Sequana project (v0.8.5) (95). First, the homogeneity of the coverage was checked with Sequana coverage (96), and only NGS runs with a coverage above 2,000× were further analyzed. Next, SNPs, insertions and deletions, and multi-nucleotide polymorphisms were detected with Freebayes (v1.3.2) using the default option except for the ploidy option, which was set at 25 (97). Variants were filtered, and only those with a Freebayes score >1, a frequency ≥5%, a minimal depth of 10, and a minimal forward and reverse strand ratio of 0.2 were retained. To exclude possible genomic reorganization, *de novo* assembly was performed with SPAdes (98) using the default options, and resulting contigs were compared to the reference sequence with the NCBI Blast2Seq tool.

## Indirect immunofluorescence

Vero-NK cells were plated on glass coverslips in 24-well plates and were infected with MV-ATU3-S or the parental MVSchw at an MOI of 0.05 or with the recombinant MV-ATU3-S2P, -S2PΔF, -S2P3F, and -S2PΔF2A at an MOI of 0.1. When syncytia were clearly visible but not yet confluent (~30 h p.i.), cells were fixed with 4% paraformaldehyde in PBS for 20 min at 4°C. Coverslips were incubated for 1 h in PBS containing 1% donkey serum (DKS), then for 1 h with rabbit anti-SARS-CoV-2 spike polyclonal antibodies diluted 1:1,000 in PBS-1% DKS. After subsequent incubation with AlexaFluor-488-conjugated anti-rabbit IgG, samples were mounted on slides in DAPI-containing ProLong solution (Invitrogen). Pictures were acquired with an inverted fluorescence microscope in the ApoTome mode (Zeiss) using a 40× objective and processed with the Fiji software (99).

## Western blot analysis

Vero-NK cells were infected with recombinant MV-ATU3 expressing S or derivatives at an MOI of 1 and incubated for 24 h at 37°C under 5%CO<sub>2</sub> or at an MOI of 0.05 for 39 h. Protein cell extracts were prepared by harvesting infected cells in lithium dodecyl sulfate buffer containing 2-mercaptoethanol, followed by heating at 95°C for 10 min and freeze thaw. Samples were denatured at 70°C for 5 min, and proteins were separated by electrophoresis on 4%–12% Nupage Novex Bis Tris gels (Invitrogen) with MOPS buffer and transferred onto PVDF membranes using iBlot 2 transfer system (Invitrogen). Membranes were blocked with PBS containing 0.1% Tween 20 and 5% skim milk, probed with anti-SARS-CoV/CoV-2 or anti-MV N polyclonal rabbit antibodies diluted 1:40,000, and finally incubated with AlexaFluor-680-conjugated anti-rabbit IgG. Conjugated antibodies were revealed using high-resolution near infra-red imaging

(Li-Cor, Odyssey CLx). Seeblue Plus2-prestained protein ladder was used as molecular mass reference.

### GFP-split fusion assay

Fusion assays were performed as described previously (44). Briefly, 293T-GFP1-10 and -GFP11 cells (1:1 ratio) were co-transfected with S (see Plasmids section), hACE2 (pcDNA3.1-hACE2), and TMPRSS2 (pCSDest-TMPRSS2) expression plasmid DNAs using Lipofectamine 2000 (Invitrogen) and plated in 96-well plates. At 18 h post-transfection, 21 images covering 90% of the well surface were acquired per well with an Opera Phenix High-Content Screening System (PerkinElmer), and the cell confluence area and the GFP area were quantified by Harmony High-Content Imaging and Analysis Software. Cell fusion was scored by calculating the percentage of GFP-positive cell area per cell confluence area. Cell-surface expression of native and mutated S was checked in parallel to the fusion assay by flow cytometry analysis of unpermeabilized transfected 293T-GFP1-10 cells using an Attune NxT Flow Cytometer (Invitrogen). Briefly, cells were incubated with anti-SARS-CoV S mouse polyclonal antibodies, then with AlexaFluor-488-conjugated anti-mouse IgG for 30 min each, then fixed for 15 min in 4% PFA. Data were analyzed with FlowJo v10.6 software (LLC, BD Life Sciences).

### Mouse immunization and challenge

All mice were bred and housed under specific pathogen-free conditions at the Institut Pasteur animal facility. Groups of 6- to 9-week-old male IFN $\alpha$ / $\beta$ R<sup>-/-</sup> (IFNAR-KO) or hCD46<sup>+/-</sup> IFN $\alpha$ / $\beta$ R<sup>-/-</sup> (CD46-IFNAR) mice in 129/Sv background (33, 100) were immunized by intraperitoneal (i.p.) injection with 10<sup>5</sup> TCID<sub>50</sub> of recombinant MV-ATU3 expressing native S or mutated S or parental MVSchw in 200  $\mu$ L PBS. Control groups of 6- to 9-week-old male 129/Sv mice were immunized by intramuscular (i.m.) injection with adjuvanted formulations containing 2  $\mu$ g of recombinant, trimerized S2P3F-T4-8HIS spike protein (see ELISA section) and 50  $\mu$ g aluminum hydroxide (Alu-Gel-S, Serva).

Booster injections were administered 4 weeks later when applicable. Blood samples were collected by retro-orbital bleeding at various time points, generally at 3 (IS1) and 7 (IS2) weeks post-initial inoculation.

For challenge with SARS-CoV-2, mice were lightly anesthetized by a mixture of ketamine (Imalgene, 50 mg/kg) and xylazine (Rompun, 10 mg/kg) and instilled intranasally with 6  $\times$  10<sup>8</sup> ICU of Ad5::hACE2 in 30  $\mu$ L PBS. Four days later, mice were anesthetized as described above and inoculated intranasally with 2  $\times$  10<sup>4</sup> PFU of SARS-CoV-2 in 30  $\mu$ L PBS. Mice were euthanized 4 days after SARS-CoV-2 challenge by cervical dislocation, and lungs were collected and processed essentially as described previously (101). Briefly, lungs were removed aseptically, rinsed extensively in PBS, and each lobe was separated into two equal parts. Halves of each lung lobe were kept on ice and ground together in 750  $\mu$ L of ice-cold PBS using a FastPrep-24 homogenizer and Lysing Matrix M tubes (MP Biomedical) by two successive pulses at 4 m/s for 20 s with incubation on ice between the two homogenization cycles. Homogenates were clarified by centrifugation for 10 min at 2,000 g at 4°C and kept at -80°C in single-use aliquots. The other half lobes were fixed for 7 days in a solution containing 4% formaldehyde in PBS, then transferred in 70% ethanol for histological analysis.

### ELISAs specific for MV and SARS-CoV-2 S

Recombinant trimerized SARS-CoV-2 spike ectodomain, further stabilized in its uncleaved prefusion state, was produced following transfection of Expi 293 F cells (Life Technologies) with pCI-S2P3F-T4-strep DNA using ExpiFectamine 293 Transfection Kit. Transfected cells were cultured for 5 days in freestyle 293 expression medium (Life Technologies) at 37°C under orbital agitation at 110 rpm, after which cell culture medium was collected and concentrated using a 100-kDa MWCO tangential flow filtration cartridge (Cytiva) with a phosphate filtration buffer (phosphate 50 mM, NaCl 300 mM,

pH 8.0). The protein was purified on a StrepTrap HP affinity column (Cytiva) using 2.5 mM desthiobiotine in filtration buffer for elution. The recombinant spike ectodomain was also produced following co-transfection of *Drosophila* S2 cells (Life Technologies) with pMT-BiP-S2P3F-T4-strep and pCoBlast (Invitrogen) and establishment of a stable cell line using blasticidin for selection. The resulting cells were cultured at 28°C for 7 days in Insect-XPRESS expression medium (Lonza) supplemented with 5  $\mu$ M CdCl<sub>2</sub>, under orbital agitation at 60 rpm, after which cell culture medium was collected, and the protein was purified as described above. For mouse immunization, a recombinant spike ectodomain with a carboxy-terminal polyhistidine tag was produced following transfection of Expi 293 F cells with pCI-S2P3F-T4-8HIS DNA, essentially as described above with the following modifications: the cell culture supernatant was concentrated as above with the phosphate filtration buffer supplemented with 20 mM imidazole, and the protein was purified on a HisTrap HP column (Cytiva) using a 0.15–0.6-M imidazole gradient in filtration buffer for elution. The recombinant spike proteins were recovered as homotrimers and analyzed in both denaturing condition by stain-free SDS-PAGE and native condition using analytical size exclusion chromatography and multi-angle diffusion light scattering for quality validation. Samples were aliquoted and stored at –80°C until use. Short-term storage was at –20°C after further dilution in glycerol (50% final concentration).

Microtiter plates (Nunc MaxiSorp, Thermo Scientific) were coated overnight at +4°C with 50 ng/well of either recombinant, trimerized S2P3F-T4-strep protein or purified Measles antigen (Jena Bioscience, # PR-BA102-S-L) and incubated for 1 h at 37°C with fourfold serial dilutions of mouse sera in PBS containing 0.1% Tween-20 (PBS-T) and 3% skimmed milk. After PBS-T washings, bound antibodies were revealed with mouse-specific anti-IgG (gamma-chain), or isotype-specific anti-IgG1 or anti-IgG2a secondary antibodies coupled to horseradish peroxidase and TMB chromogenic substrate (3,3',–5,5'-tetramethylbenzidine, SeraCare Life Sciences). Following a 10-min incubation, reaction was stopped by adding 100  $\mu$ L/well of 2N H<sub>2</sub>SO<sub>4</sub>, and optical densities were measured at 450 nm/620 nm with an Infinite F50 reader (Tecan). ELISA IgG titers were calculated as the reciprocal of the highest dilution of serum yielding an absorbance of 0.5. This threshold lies in the linear portion of the titration curve (plot of absorbance versus log<sub>10</sub> of the serum dilution) and yields highly sensitive and reproducible antibody titers.

### SARS-CoV-2 microneutralization assays

Two- or threefold serial dilutions of heat-inactivated (56°C, 30 min) mouse or human serum samples in DTB were incubated for 2 h at 37°C with 20 TCID<sub>50</sub> of SARS-CoV-2 in a final volume of 50  $\mu$ L. Mixtures were then added to subconfluent monolayers of FRhK-4 cells plated in DMEM-5 in 96-well plates, and infected cells were incubated at 37°C under 5% CO<sub>2</sub>. Each serum dilution was assayed in quadruplicates, and CPE endpoints were scored in individual wells up to 5 days p.i. Neutralizing antibody titers 95 (NT95) were determined according to the Reed and Muench method (102) as the reciprocal of the highest dilution of serum which prevented CPE in at least 50% of the four wells.

In some experiments, convalescent human sera were used as reference. These sera included a very high-titer reference serum (20/130) (103) and panel 20/118 (104) comprising low-titer (20/124, 20/126), medium-titer (20/122), high-titer serum (20/120) and a negative plasma pool (20/128) from healthy donors, all made available by NIBSC in April 2020. In late 2020, the 20/130 reference serum has been characterized in the collaborative study for the establishment of the First WHO International Standard for anti-SARS-CoV-2 immunoglobulin, and its potency was calculated to be 1,300 IU/mL (105).

### Determination of SARS-CoV-2 loads in mouse lungs

SARS-CoV-2 genomic RNA loads in mouse lungs were determined by extracting viral RNA from 70  $\mu$ L of lung homogenate using QIAamp Viral RNA Mini Kit (Qiagen). To

remove non-particulate viral RNA in lung homogenates, 70  $\mu$ L samples were treated with 100U RNaseI (Ambion) for 30 min at 37°C prior to inactivation with the AVL buffer of the QIAamp Viral RNA Mini Kit. Viral loads (expressed as genome equivalents per lung) were determined following reverse transcription and real-time quantitative PCR essentially as described by Corman et al. (106), using SuperScript III Platinum One-Step Quantitative RT-PCR System (Invitrogen) and primers and probe (Eurofins) targeting SARS-CoV-2 envelope (E) gene as listed in Table S2. *In vitro* transcribed RNA derived from the cloned SARS-CoV E gene was synthesized using T7 RiboMAX Express Large Scale RNA production system (Promega), then purified by phenol/chloroform extractions and two successive precipitations with ethanol (107). RNA quality was controlled on Agilent 2100 bioanalyzer\_Eukaryote Total RNA Nano Series II. RNA concentration was determined by optical density measurement. RNA was then diluted to  $10^9$  molecules/ $\mu$ L in RNase-free water containing 100  $\mu$ g/mL tRNA carrier and stored in single-use aliquots at  $-80^\circ\text{C}$ . Serial dilutions of this *in vitro*-transcribed RNA were prepared in RNase-free water containing 10  $\mu$ g/mL tRNA carrier and used to establish a standard curve in each assay. Thermal cycling conditions were as follows: (i) reverse transcription at 55°C for 10 min, (ii) enzyme inactivation at 95°C for 3 min, (iii) 45 cycles of denaturation/amplification at 95°C for 15 s, 58°C for 30 s. Products were analyzed on an ABI 7500 Fast real-time PCR system (Applied Biosystems).

Infectious SARS-CoV-2 loads in mouse lungs were determined by PFU assay in Vero-NK cells seeded in 12-well plates. Confluent monolayers in duplicate wells were infected for 1 h at 37°C under 5%  $\text{CO}_2$  with fivefold serial dilutions of lung homogenates in DTB. Following withdrawal of viral inoculum, cells were placed in a gelled medium composed of complete DMEM containing 1  $\mu$ g/mL TPCK-treated trypsin (Worthington) and 1.2% Avicel RCS81 (FMC Biopolymer) and further incubated at 37°C for 72 h. Cell sheets were then fixed and stained with 0.1% crystal violet, 4% formaldehyde, 20% ethanol solution, and plaques were counted. Infectious viral titers were expressed as PFU per lung.

### Histopathology and immunohistochemistry

Fixed lung samples were embedded in paraffin. Paraffin sections (5  $\mu$ m thick) were processed for routine histology using hematoxylin and eosin. Histological changes were qualitatively described. Inflammation (interstitial pneumonia) and histopathological (bronchiolar) lesions were scored, using a five-scale severity grade (1: minimal, 2: mild, 3: moderate, 4: marked, and 5: severe), reflecting severity and extent of the lesions and alterations of the lung structure. Scoring for a given mouse was performed in sections of each lobe, and the arithmetic mean of scores found in the five lobes was calculated.

In some cases, serial sections were prepared for immunohistochemistry analyses. Antigen retrieval was performed by heating at 100°C for 20 min in a pH 6.0 citrate buffer (AR9961, Leica). Next, IHC was performed by using the Bond RX robot (Leica) with rabbit anti - SARS-CoV - 2 nucleoprotein antibody (NB100 - 56576, Novus Biologicals), biotinylated goat anti - rabbit Ig secondary antibody (E0432, Dako, Agilent), and streptavidine-HRP/DAB detection system (DS9263, Leica).

All slides were scanned using the AxioScan Z1 (Zeiss) system, and images were analyzed with the Zen 2.6 software.

### MV and SARS-CoV-2 ELISpot assays

Spleens from immunized or control mice were harvested, and single-cell suspensions of splenocytes were prepared by gentle grinding over 70  $\mu$ m pore sieves (Becton Dickinson). Red blood cells were removed by treatment with ACK lysing buffer (Invitrogen). After extensive washing with complete RPMI-10 medium (RPMI 1640 supplemented with 10% FBS, 10 mM HEPES,  $5 \times 10^{-5}$  M 2-mercaptoethanol, non-essential amino acids, sodium pyruvate, 100 U/mL penicillin, and 100  $\mu$ g/mL streptomycin) and filtration through 40  $\mu$ m pore sieves, viable splenocytes were enumerated using a Luna FL counter and a fluorescent dye mixture (Logos Biosystems). The frequency

of MV and SARS-CoV-2-specific IFN- $\gamma$ -producing T cells was quantified in a standard ELISpot assay. Briefly, 96-well Multi-screen PVDF plates (Millipore) were coated with 0.5  $\mu\text{g}/\text{well}$  rat anti-mouse IFN- $\gamma$  antibodies (AN18, Becton-Dickinson, # 551309) in PBS. Plates were blocked by a 2-h incubation with complete RPMI-10. Various numbers of splenocytes (typically  $4 \times 10^5$ ,  $2 \times 10^5$ , and  $1 \times 10^5/\text{well}$ ) were then plated in triplicate in the presence or absence of appropriate peptide pools or individual peptides at 1–10  $\mu\text{M}$  final concentration and of 10 U/mL IL-2 (Miltenyi Biotec). Cells were incubated for 20 h at 37°C, and after extensive washes, the spots were revealed by successive incubations with biotinylated rat anti-mouse IFN- $\gamma$  antibodies (R46A2, Becton-Dickinson, # 551506), alkaline phosphatase-conjugated streptavidin (Becton-Dickinson, # 554065), and 5-bromo-4-chloro-3-indolylphosphate/nitroblue tetrazolium (NBT/BCIP, Sigma) as the chromogenic substrate. The spots were counted using an automated ImmunoSpot analyzer and associated Biospot 7.0 software (CTL). For each mouse, the number of peptide-specific IFN- $\gamma$ -producing cells was determined by calculating the difference between the number of spots generated in the presence of a negative control peptide and of the specific peptide. Results were expressed as the number of spot-forming cells per  $10^6$  splenocytes.

In order to determine the responses against the SARS-CoV-2 spike protein, T cells were stimulated at a total concentration of 10  $\mu\text{M}$  with peptide pools spanning the S1 and S2 domains, respectively, containing 15 amino acid peptides with 10 residues overlaps (Mimotopes). These pools contained 135 and 118 peptides, respectively, and were prepared in medium by mixing individual peptides dissolved in DMSO at a concentration of 2 mg/mL. In order to map the immunodominant peptides, a series of pools of eight peptides were used to stimulate T cells. Positive pools were deconvoluted by testing all peptides individually.

The measles H22-30 (RIVINREHL) and H446-454 (SNHNNVYWL) peptides and the influenza nucleoprotein NP366 (SCOT) peptide (ASNENMDTM) were synthesized by Eurogentec and used at a concentration of 1  $\mu\text{M}$  each, as positive (pooled MV peptides) and negative control peptides, respectively.

### Intracellular cytokine staining assays

Splenocytes were cultured at  $10^6$  cells/well in 96-well plates in IMDM with Glutamax (ThermoFisher) containing 10% FBS, 1% penicillin-streptomycin, 10 U/mL IL-2 (Miltenyi Biotec), and 100 ng/mL IL-7 (Miltenyi Biotec). Cells were stimulated for 6 h at 37°C with peptide pools spanning the S1 and S2 domains (see ELISpot section) at a total concentration of 10  $\mu\text{g}/\text{mL}$  (6.7  $\mu\text{M}$ ). BD GolgiPlug and BD GolgiStop (BD Biosciences) were added for the final 4 h. The MV peptide pool was used at a concentration of 1  $\mu\text{M}$  each. For positive controls, cells were stimulated with 50 ng/mL PMA (Sigma Aldrich) and 1  $\mu\text{g}/\text{mL}$  Ionomycin (Sigma Aldrich). For negative controls, medium with DMSO was used. Cells were incubated with mouse Fc receptor block (anti-mouse 24G2) and Fixable viability dye eFluor506 (eBioscience) to exclude dead cells. Cells were stained with  $\alpha$ -CD45 BV395 (BD Pharmingen # 564279),  $\alpha$ -CD19 AF700 (eBioscience # 56-0193-80),  $\alpha$ -CD11b AF700 (eBioscience # 56-0112-82),  $\alpha$ -CD11c AF700 (eBioscience # 56-0114-82),  $\alpha$ -CD3e BV650 (BD Pharmingen # 564378),  $\alpha$ -CD4 eFluor 450 (eBioscience # 48-0041-80), and  $\alpha$ -CD8a PerCp Cy5.5 (BD Pharmingen # 5511622). Following fixation and permeabilization (Cytofix/Cytoperm, BD Biosciences # 555029), cells were stained intracellularly with  $\alpha$ -TNF-FITC (eBioscience # 11-7321-81),  $\alpha$ -IFN- $\gamma$  PE-Cy7 (BD Pharmingen # 55764),  $\alpha$ -IL-5 PE (eBioscience # 12-7052-82), and  $\alpha$ -IL-13 eFluor 660 (eBioscience # 50-7133-82). Cells were acquired by flow cytometry using a Fortessa system (BD Biosciences), and data were analyzed with FlowJo v10.7 software (LLC, BD Life Sciences). T cells were selected as positive for CD45 and CD3e and negative for CD19, CD-11b, CD-11c, and further differentiated into CD4<sup>+</sup> and CD8<sup>+</sup> T cells for the cytokine analysis.

## Statistical analyses

Data were expressed as medians and in some indicated instances, either as geometric means (with geometric standard deviations) of the raw values or as means  $\pm$  SD of  $\log_{10}$  values, and the exact numbers ( $n$ ) of mice per group are annotated in the corresponding figure legend. Statistical analysis of virological and immunological data were performed using Prism v9.2 (GraphPad Software). Differences between two groups were evaluated by using unpaired two-tailed non-parametric Mann-Whitney U test. For statistical analysis of multiple groups, the Kruskal-Wallis test followed by Dunn's uncorrected analysis was applied. Where indicated, ANOVA and uncorrected Fisher's LSD test were applied on the  $\log_{10}$  values measured for individual mice, with the assumption used for small samples (normal distribution of the variables and same variance for the populations to be compared).

Values of  $P < 0.05$  were considered significant, and levels of significance are indicated on the graphs by asterisks: \* $P < 0.05$ ; \*\* $P < 0.005$ ; \*\*\* $P < 0.0005$ ; and \*\*\*\* $P < 0.0001$ .

## Material availability

Unique biological materials used in this study are available from commercial sources where indicated or from the corresponding authors, upon reasonable request. Plasmids or recombinant viruses may require filing of material transfer agreements.

## ACKNOWLEDGMENTS

Funding for the work was granted to Institut Pasteur by the Coalition for Epidemic Preparedness Innovations (CEPI, <https://cepi.net>) as part of the project "Outbreak Response to Novel Coronavirus (COVID-19): Development of a vaccine against novel coronavirus SARS-CoV-2 using the clinical Phase III measles vector technology", led by C.G. and N.E. In addition, we thank the CEPI project team for their continuous support and helpful discussions.

This work was also supported by grants to N.E. from Institut Pasteur (<https://www.pasteur.fr>), including the "URGENCE COVID-19" fundraising campaign of Institut Pasteur. H.T. and P.F. were recipients of a post-doctoral fellowship from the ANRS|Maladies infectieuses Emergentes (<https://www.anrs.fr>); H.T. also received a fellowship from RECOVER, a project funded by the European Union's Horizon 2020 research and innovation programme (<https://ec.europa.eu/programmes/horizon2020>) under grant agreement No. 101003589. E.S. was the recipient of a doctoral contract at the BioSPC-ED562, Université Paris Cité (<https://ecolesdoctorales.parisdescartes.fr/ed157>).

The funders played no role in study design, data collection, analysis and interpretation of data, decision to publish, or the preparation of this manuscript.

The COVID-19 convalescent plasma panel (NIBSC 20/118) and the reference high-titer convalescent plasma (NIBSC 20/130) were obtained from the National Institute for Biological Standards and Control, UK.

The authors are grateful to Christian Mandl (Themis Bioscience Scientific Advisory Board), Katrin Ramsauer, Roland Tschismarov, Sabrina Schrauf, Georg Hinterkörner, Matthias Müllner, Jochen Stritzker (Themis Bioscience, Austria), Anita McElroy, Linda Murphy (University of Pittsburgh, PA, USA), Sylvie van der Werf, Félix Rey, and Olivier Schwartz (Institut Pasteur, France) for helpful discussions and critical reading of the manuscript. The authors thank Christophe d'Enfert and Isabelle Buckle (Institut Pasteur, France) for their continuous support throughout the realization of this study. The authors thank the efforts of Nathalie Denoyes and the Institut Pasteur Department of Risk Prevention for timely regulatory and logistical assistance with this work under the pandemic conditions. The authors also thank Sylvie van der Werf and the members of the National Reference Centre for Viruses of Respiratory Infections (Institut Pasteur, France) for providing the Beta-CoV/France/IDF0372/2020 SARS-CoV-2 clinical isolate, supplied through the European Virus Archive Global (Evag), a project that has received funding from the European Union's Horizon 2020 program (<https://>

[ec.europa.eu/programmes/horizon2020](https://ec.europa.eu/programmes/horizon2020)) under grant agreement no. 653316; Amandine Noirat and Fabien Le Chevalier (Pasteur-TheraVectys Joint Lab) for help in producing the Ad5::hACE2 vector and in analyzing the ICS data, respectively; Etienne Simon-Lorière (Evolutionary Genomics of RNA Viruses) and the team of the Mutualized Platform for Microbiology (Institut Pasteur) for help with whole genome sequencing of the SARS-CoV-2 passages; François Déjardin (PF3PR core facility, Institut Pasteur), Patrick England and the staff of the PFBMI core facility (Institut Pasteur) for help in producing and validating the recombinant spike proteins; Pierre Lafaye (Antibody Engineering core facility, Institut Pasteur) for help in preparing the rabbit antibodies against SARS-CoV-2 spike protein; Magali Tichit, Mélanie Juchet-Martin, and Sarra Loulizi (Histology platform, Institut Pasteur) for the technical processing of histological samples; Angeliki-Anna Beka for help with immunofluorescence microscopy; Marion Bérard, Maryline Bourguine, Pierre Authié, Laetitia Breton, Rachid Chennouf, and Eddie Maranghi for help in implementing experiments at the Institut Pasteur animal facilities.

Study concept and design, N.E., C.G., A.M., W.P.D., and L.Maj.; construction of measles-vectored vaccine candidates, J.Bru., Z.C., M.G., A.M., and N.E.; acquisition of data, J.Bru., Z.C., M.G., H.T., J.Buch., P.F., J.L., D.B., L.Ma., E.S., D.H., H.S.-M., L.Maj., A.M., and N.E.; analysis and interpretation of data, J.Bru., Z.C., M.G., J.Buch., F.G., H.S.-M., M.M., L.Maj., C.G., A.M., and N.E.; Ad5::hACE2 vector, M.-W.K., P.C., and L.Maj.; recombinant S proteins, M.G., E.D., S.P., and N.E.; writing of the manuscript, A.M., C.G., and N.E.; review and editing of the manuscript, J.Bru., Z.C., M.G., F.G., L.Maj., W.P.D., C.G., A.M., and N.E. All authors approved the final version of the manuscript.

## AUTHOR AFFILIATIONS

<sup>1</sup>Institut Pasteur, Université Paris Cité, Département de Santé Globale, Paris, France

<sup>2</sup>Institut Pasteur, Université Paris Cité, CNRS UMR3569, Génétique Moléculaire des Virus à ARN, Paris, France

<sup>3</sup>Institut Pasteur, Université Paris Cité, Pasteur-TheraVectys Joint Lab, Paris, France

<sup>4</sup>Institut Pasteur, Université Paris Cité, CNRS UMR3569, Virus and Immunity Unit, Paris, France

<sup>5</sup>Institut Pasteur, Université Paris Cité, INSERM U1223, Innate Immunity Unit, Paris, France

<sup>6</sup>Institut Pasteur, Université Paris Cité, Biomics, C2RT, Paris, France

<sup>7</sup>Institut Pasteur, Université Paris Cité, CNRS UMR 3528, Production and Purification of Recombinant Proteins Technological Platform, Paris, France

<sup>8</sup>Institut Pasteur, Université Paris Cité, Histopathology Platform, Paris, France

<sup>9</sup>Institut Pasteur, Université Paris Cité, INSERM U1223, Lymphocytes and Immunity Unit, Paris, France

<sup>10</sup>Center for Vaccine Research, Department of Microbiology and Molecular Genetics, University of Pittsburgh, Pittsburgh, Pennsylvania, USA

<sup>11</sup>Institut Pasteur, Université Paris Cité, Innovation Office, Vaccine Programs, Paris, France

## PRESENT ADDRESS

Marion Gransagne, Synthelis, La Tronche, France

Houda Tabbal, GSK, Mississauga, Ontario, Canada

Min-Wen Ku, Wyss Institute at Harvard University, Boston, Massachusetts, USA

Priyanka Fernandes, Cherry Biotech Innovation, Paris, France

Emeline Simon, ANRS | Maladies infectieuses émergentes, Paris, France

Christiane Gerke, International Vaccine Institute (IVI), Europe Regional Office, Stockholm, Sweden

## AUTHOR ORCIDs

W. Paul Duprex  <http://orcid.org/0000-0003-1716-6376>

Christiane Gerke  <http://orcid.org/0000-0001-9446-8031>

Annette Martin  <http://orcid.org/0000-0002-3054-3925>

Nicolas Escriou  <http://orcid.org/0000-0002-1224-6839>

## FUNDING

Funder	Grant(s)	Author(s)
Institut Pasteur	URGENCE COVID-19	Nicolas Escriou
Agence Nationale de la Recherche (ANR)	2 post-doctoral fellowships	Houda Tabbal Priyanka Fernandes
EC   Horizon 2020 Framework Programme (H2020)	101003589 (post-doctoral fellowship)	Houda Tabbal
Université Sorbonne Paris Cité (USPC)	doctoral fellowship	Emeline Simon
Coalition for Epidemic Preparedness Innovations (CEPI)	Outbreak Response to Novel Coronavirus (COVID-19): Development of a vaccine against novel coronavirus SARS-CoV-2 using the clinical Phase III measles vector technology	Christiane Gerke Nicolas Escriou

## AUTHOR CONTRIBUTIONS

Jérémy Brunet, Formal analysis, Investigation, Writing – review and editing | Zaineb Choucha, Formal analysis, Investigation, Writing – review and editing | Marion Gransagne, Formal analysis, Investigation, Writing – review and editing | Houda Tabbal, Investigation | Min-Wen Ku, Methodology, Resources | Julian Buchrieser, Formal analysis, Investigation | Priyanka Fernandes, Investigation | Damien Batalie, Investigation | Jodie Lopez, Investigation | Laurence Ma, Investigation | Evelyne Dufour, Resources | Emeline Simon, Investigation | David Hardy, Investigation | Stéphane Petres, Resources | Françoise Guinet, Formal analysis, Writing – review and editing | Helene Strick-Marchand, Formal analysis, Investigation | Marc Monot, Formal analysis, Methodology | Pierre Charneau, Methodology, Resources | Laleh Majlessi, Conceptualization, Formal analysis, Investigation, Methodology, Writing – review and editing | W. Paul Duprex, Conceptualization, Writing – review and editing | Christiane Gerke, Conceptualization, Formal analysis, Funding acquisition, Project administration, Writing – original draft, Writing – review and editing | Annette Martin, Conceptualization, Formal analysis, Investigation, Methodology, Writing – original draft, Writing – review and editing, Supervision | Nicolas Escriou, Conceptualization, Formal analysis, Funding acquisition, Investigation, Supervision, Writing – original draft, Writing – review and editing, Project administration

## DATA AVAILABILITY

All data generated and analyzed during this study are included in the published article and its supplemental files.

## ETHICS APPROVAL

All experiments were approved by the Safety, Animal Care and Use Committee at Institut Pasteur and conducted in compliance with European and French animal welfare regulations. The study protocol was authorized by the French Ministry of Higher Education, Research and Innovation, following a favorable recommendation from Institut Pasteur's local ethics committee (CETEA n°089).

## ADDITIONAL FILES

The following material is available [online](#).

## Supplemental Material

Supplemental material (JV101693-23-s0001.pdf). Tables S1 and S2, Figures S1 to S5, and supplemental method.

## REFERENCES

- Zhou P, Yang XL, Wang XG, Hu B, Zhang L, Zhang W, Si HR, Zhu Y, Li B, Huang CL, et al. 2020. A pneumonia outbreak associated with a new coronavirus of probable bat origin. *Nature* 579:270–273. <https://doi.org/10.1038/s41586-020-2012-7>
- Zhu N, Zhang D, Wang W, Li X, Yang B, Song J, Zhao X, Huang B, Shi W, Lu R, Niu P, Zhan F, Ma X, Wang D, Xu W, Wu G, Gao GF, Tan W, China Novel Coronavirus Investigating and Research Team. 2020. A novel coronavirus from patients with pneumonia in China, 2019. *N Engl J Med* 382:727–733. <https://doi.org/10.1056/NEJMoa2001017>
- World Health Organization. 2023. WHO COVID-19 dashboard. Available from: <https://covid19.who.int>. Retrieved 27 Jul 2023.
- World Health Organization. 2023. WHO director-general's opening remarks at the media briefing. Available from: <https://www.who.int/news-room/speeches/item/who-director-general-s-opening-remarks-at-the-media-briefing---5-may-2023>. Retrieved 27 Jul 2023.
- BastaNE, Moodie EMM, on behalf of the VIPER (Vaccines IdP, and Epidemiology Research) Group COVID-19 Vaccine Development and Approvals Tracker Team. 2022. COVID-19 vaccine development and approvals tracker. Available from: <https://covid19.trackvaccines.org/vaccines/approved/#vaccine-list>. Retrieved 27 Jul 2023.
- World Health Organization. 2023. COVID-19 vaccines with WHO emergency use listing. Available from: <https://extranet.who.int/pqweb/vaccines/vaccinescovid-19-vaccine-eul-issued>. Retrieved 27 Jul 2023.
- Biancolella M, Colona VL, Luzzatto L, Watt JL, Mattiuz G, Conticello SG, Kaminski N, Mehriani-Shai R, Ko AI, Gonsalves GS, Vasiliou V, Novelli G, Reichardt JKV. 2023. COVID-19 annual update: a narrative review. *Hum Genomics* 17:68. <https://doi.org/10.1186/s40246-023-00515-2>
- Drosten C, Preiser W, Günther S, Schmitz H, Doerr HW. 2003. Severe acute respiratory syndrome: identification of the etiological agent. *Trends Mol Med* 9:325–327. [https://doi.org/10.1016/s1471-4914\(03\)00133-3](https://doi.org/10.1016/s1471-4914(03)00133-3)
- Ksiazek TG, Erdman D, Goldsmith CS, Zaki SR, Peret T, Emery S, Tong S, Urbani C, Comer JA, Lim W, et al. 2003. A novel coronavirus associated with severe acute respiratory syndrome. *N Engl J Med* 348:1953–1966. <https://doi.org/10.1056/NEJMoa030781>
- Zaki AM, van Boheemen S, Bestebroer TM, Osterhaus ADME, Fouchier RAM. 2012. Isolation of a novel coronavirus from a man with pneumonia in Saudi Arabia. *N Engl J Med* 367:1814–1820. <https://doi.org/10.1056/NEJMoa1211721>
- Raj VS, Osterhaus A, Fouchier RAM, Haagmans BL. 2014. MERS: emergence of a novel human coronavirus. *Curr Opin Virol* 5:58–62. <https://doi.org/10.1016/j.coviro.2014.01.010>
- Jackson CB, Farzan M, Chen B, Choe H. 2022. Mechanisms of SARS-CoV-2 entry into cells. *Nat Rev Mol Cell Biol* 23:3–20. <https://doi.org/10.1038/s41580-021-00418-x>
- Walls AC, Park YJ, Tortorici MA, Wall A, McGuire AT, Velesler D. 2020. Structure, function, and antigenicity of the SARS-CoV-2 spike glycoprotein. *Cell* 181:281–292. <https://doi.org/10.1016/j.cell.2020.02.058>
- Wrapp D, Wang N, Corbett KS, Goldsmith JA, Hsieh C-L, Abiona O, Graham BS, McLellan JS. 2020. Cryo-EM structure of the 2019-nCoV spike in the prefusion conformation. *Science* 367:1260–1263. <https://doi.org/10.1126/science.abb2507>
- Xia X. 2021. Domains and functions of spike protein in SARS-CoV-2 in the context of vaccine design. *Viruses* 13:109. <https://doi.org/10.3390/v13010109>
- Hoffmann M, Kleine-Weber H, Pöhlmann S. 2020. A multibasic cleavage site in the spike protein of SARS-CoV-2 is essential for infection of human lung cells. *Mol Cell* 78:779–784. <https://doi.org/10.1016/j.molcel.2020.04.022>
- Millet JK, Whittaker GR. 2014. Host cell entry of middle east respiratory syndrome coronavirus after two-step, furin-mediated activation of the spike protein. *Proc Natl Acad Sci U S A* 111:15214–15219. <https://doi.org/10.1073/pnas.1407087111>
- Ou X, Liu Y, Lei X, Li P, Mi D, Ren L, Guo L, Guo R, Chen T, Hu J, Xiang Z, Mu Z, Chen X, Chen J, Hu K, Jin Q, Wang J, Qian Z. 2020. Characterization of spike glycoprotein of SARS-CoV-2 on virus entry and its immune cross-reactivity with SARS-CoV. *Nat Commun* 11:1620. <https://doi.org/10.1038/s41467-020-15562-9>
- Hoffmann M, Kleine-Weber H, Schroeder S, Krüger N, Herrler T, Erichsen S, Schiergens TS, Herrler G, Wu N-H, Nitsche A, Müller MA, Drosten C, Pöhlmann S. 2020. SARS-CoV-2 cell entry depends on ACE2 and TMPRSS2 and is blocked by a clinically proven protease inhibitor. *Cell* 181:271–280. <https://doi.org/10.1016/j.cell.2020.02.052>
- Peacock TP, Goldhill DH, Zhou J, Baillon L, Frise R, Swann OC, Kugathasan R, Penn R, Brown JC, Sanchez-David RY, Braga L, Williamson MK, Hassard JA, Staller E, Hanley B, Osborn M, Giacca M, Davidson AD, Matthews DA, Barclay WS. 2021. The furin cleavage site in the SARS-CoV-2 spike protein is required for transmission in ferrets. *Nat Microbiol* 6:899–909. <https://doi.org/10.1038/s41564-021-00908-w>
- Suthar MS, Zimmerman MG, Kauffman RC, Mantus G, Linderman SL, Hudson WH, Vanderheiden A, Nyhoff L, Davis CW, Adekunle O, et al. 2020. Rapid generation of neutralizing antibody responses in COVID-19 patients. *Cell Rep Med* 1:100040. <https://doi.org/10.1016/j.xcrm.2020.100040>
- Shrock E, Fujimura E, Kula T, Timms RT, Lee I-H, Leng Y, Robinson ML, Sie BM, Li MZ, Chen Y, et al. 2020. Viral epitope profiling of COVID-19 patients reveals cross-reactivity and correlates of severity. *Science* 370:eabd4250. <https://doi.org/10.1126/science.abd4250>
- Khoury DS, Cromer D, Reynaldi A, Schlub TE, Wheatley AK, Juno JA, Subbarao K, Kent SJ, Triccas JA, Davenport MP. 2021. Neutralizing antibody levels are highly predictive of immune protection from symptomatic SARS-CoV-2 infection. *Nat Med* 27:1205–1211. <https://doi.org/10.1038/s41591-021-01377-8>
- Brasu N, Elia I, Russo V, Montacchiesi G, Stabile SA, De Intinis C, Fesi F, Gizzi K, Macagno M, Montone M, Mussolin B, Grifoni A, Faravelli S, Marchese S, Forneris F, De Francesco R, Sette A, Barnaba V, Sottile A, Sapino A, Pace L. 2022. Memory CD8<sup>+</sup> T cell diversity and B cell responses correlate with protection against SARS-CoV-2 following mRNA vaccination. *Nat Immunol* 23:1445–1456. <https://doi.org/10.1038/s41590-022-01313-z>
- Graham RL, Donaldson EF, Baric RS. 2013. A decade after SARS: strategies for controlling emerging coronaviruses. *Nat Rev Microbiol* 11:836–848. <https://doi.org/10.1038/nrmicro3143>
- Escriviou N, Callendret B, Lorin V, Combredet C, Marianneau P, Février M, Tangy F. 2014. Protection from SARS coronavirus conferred by live measles vaccine expressing the spike glycoprotein. *Virology* 452:453:32–41. <https://doi.org/10.1016/j.viro.2014.01.002>
- Malczyk AH, Kupke A, Prüfer S, Scheuplein VA, Hutzler S, Kreuz D, Beissert T, Bauer S, Hubich-Rau S, Tondera C, Eldin HS, Schmidt J, Vergara-Alert J, Süzer Y, Seifried J, Hanschmann K-M, Kalinke U, Herold S, Sahin U, Cichutek K, Waibler Z, Eickmann M, Becker S, Mühlebach MD. 2015. A highly immunogenic and protective Middle East respiratory syndrome coronavirus vaccine based on a recombinant measles virus vaccine platform. *J Virol* 89:11654–11667. <https://doi.org/10.1128/JVI.01815-15>
- Yong CY, Ong HK, Yeap SK, Ho KL, Tan WS. 2019. Recent advances in the vaccine development against Middle East respiratory syndrome-coronavirus. *Front Microbiol* 10:1781. <https://doi.org/10.3389/fmicb.2019.01781>
- Mistry P, Barmania F, Mellet J, Peta K, Strydom A, Viljoen IM, James W, Gordon S, Pepper MS. 2021. SARS-CoV-2 variants, vaccines, and host immunity. *Front Immunol* 12:809244. <https://doi.org/10.3389/fimmu.2021.809244>

30. Teijaro JR, Farber DL. 2021. COVID-19 vaccines: modes of immune activation and future challenges. *Nat Rev Immunol* 21:195–197. <https://doi.org/10.1038/s41577-021-00526-x>
31. Radecke F, Spielhofer P, Schneider H, Kaelin K, Huber M, Dötsch C, Christiansen G, Billeter MA. 1995. Rescue of measles viruses from cloned DNA. *EMBO J* 14:5773–5784. <https://doi.org/10.1002/j.1460-2075.1995.tb00266.x>
32. Singh M, Cattaneo R, Billeter MA. 1999. A recombinant measles virus expressing hepatitis B virus surface antigen induces humoral immune responses in genetically modified mice. *J Virol* 73:4823–4828. <https://doi.org/10.1128/JVI.73.6.4823-4828.1999>
33. Combredet C, Labrousse V, Mollet L, Lorin C, Delebecque F, Hurtrel B, McClure H, Feinberg MB, Brahic M, Tangy F. 2003. A molecularly cloned Schwarz strain of measles virus vaccine induces strong immune responses in macaques and transgenic mice. *J Virol* 77:11546–11554. <https://doi.org/10.1128/jvi.77.21.11546-11554.2003>
34. Reisinger EC, Tschismarov R, Beubler E, Wiedermann U, Firbas C, Loebermann M, Pfeiffer A, Muellner M, Tauber E, Ramsauer K. 2019. Immunogenicity, safety, and tolerability of the measles-vectored chikungunya virus vaccine MV-CHIK: a double-blind, randomised, placebo-controlled and active-controlled phase 2 trial. *Lancet* 392:2718–2727. [https://doi.org/10.1016/S0140-6736\(18\)32488-7](https://doi.org/10.1016/S0140-6736(18)32488-7)
35. Griffin DE. 2018. Measles vaccine. *Viral Immunol* 31:86–95. <https://doi.org/10.1089/vim.2017.0143>
36. Ramsauer K, Schwameis M, Firbas C, Müllner M, Putnak RJ, Thomas SJ, Desprès P, Tauber E, Jilma B, Tangy F. 2015. Immunogenicity, safety, and tolerability of a recombinant measles-virus-based chikungunya vaccine: a randomised, double-blind, placebo-controlled, active-comparator, first-in-man trial. *Lancet Infect Dis* 15:519–527. [https://doi.org/10.1016/S1473-3099\(15\)70043-5](https://doi.org/10.1016/S1473-3099(15)70043-5)
37. Nambulli S, Escriou N, Rennick LJ, Demers MJ, Tilston-Lunel NL, McElroy AK, Barbeau DJ, Crossland NA, Hoehel RM, Schrauf S, White AG, Borish HJ, Tomko JA, Frye LJ, Scanga CA, Flynn JL, Martin A, Gerke C, Hartman AL, Duprex WP. 2024. A measles-vectored vaccine candidate expressing prefusion-stabilized SARS-CoV-2 spike protein brought to phase I/II clinical trials: protection of African green monkeys from COVID-19 disease. *J Virol* 98:e1762-23. <https://doi.org/10.1128/jvi.01762-23>
38. Vanhoutte F, Liu W, Wiedmann RT, Haspelslagh L, Cao X, Boundy K, Aliprantis A, Davila M, Hartzel J, Li J, McGuire M, Ramsauer K, Tomberger Y, Tschismarov R, Brown DD, Xu W, Sachs JR, Russell K, Stoch SA, Lai E. 2022. Safety and immunogenicity of the measles vector-based SARS-CoV-2 vaccine candidate, V591, in adults: results from a phase 1/2 randomised, double-blind, placebo-controlled, dose-ranging trial. *EBioMedicine* 75:103811. <https://doi.org/10.1016/j.ebiom.2021.103811>
39. Launay O, Artaud C, Lachâtre M, Ait-Ahmed M, Klein J, Luong Nguyen LB, Durier C, Jansen B, Tomberger Y, Jolly N, Grossmann A, Tabbal H, Brunet J, Gransagne M, Choucha Z, Batalie D, Delgado A, Müllner M, Tschismarov R, Berghmans P-J, Martin A, Ramsauer K, Escriou N, Gerke C. 2022. Safety and Immunogenicity of a measles-vectored SARS-CoV-2 vaccine candidate, V591 / TMV-083, in healthy adults: results of a randomized, placebo-controlled phase I study. *EBioMedicine* 75:103810. <https://doi.org/10.1016/j.ebiom.2021.103810>
40. Callendret B, Lorin V, Charneau P, Marianneau P, Contamin H, Betton J-M, van der Werf S, Escriou N. 2007. Heterologous viral RNA export elements improve expression of severe acute respiratory syndrome (SARS) coronavirus spike protein and protective efficacy of DNA vaccines against SARS. *Virology* 363:288–302. <https://doi.org/10.1016/j.virol.2007.01.012>
41. McLellan JS, Chen M, Joyce MG, Sastry M, Stewart-Jones GBE, Yang Y, Zhang B, Chen L, Srivatsan S, Zheng A, et al. 2013. Structure-based design of a fusion glycoprotein vaccine for respiratory syncytial virus. *Science* 342:592–598. <https://doi.org/10.1126/science.1243283>
42. Pallesen J, Wang N, Corbett KS, Wrapp D, Kirchdoerfer RN, Turner HL, Cottrell CA, Becker MM, Wang L, Shi W, Kong WP, Andres EL, Kettenbach AN, Denison MR, Chappell JD, Graham BS, Ward AB, McLellan JS. 2017. Immunogenicity and structures of a rationally designed prefusion MERS-CoV spike antigen. *Proc Natl Acad Sci U S A* 114:E7348–E7357. <https://doi.org/10.1073/pnas.1707304114>
43. Kirchdoerfer RN, Wang N, Pallesen J, Wrapp D, Turner HL, Cottrell CA, Corbett KS, Graham BS, McLellan JS, Ward AB. 2018. Stabilized coronavirus spikes are resistant to conformational changes induced by receptor recognition or proteolysis. *Sci Rep* 8:15701. <https://doi.org/10.1038/s41598-018-34171-7>
44. Buchrieser J, Dufloo J, Hubert M, Monel B, Planas D, Rajah MM, Planchais C, Porrot F, Guivel-Benhassine F, Van der Werf S, Casartelli N, Mouquet H, Bruel T, Schwartz O. 2020. Syncytia formation by SARS-CoV-2-infected cells. *EMBO J* 39:e106267. <https://doi.org/10.15252/emboj.2020106267>
45. Ujiike M, Huang C, Shirato K, Makino S, Taguchi F. 2016. The contribution of the cytoplasmic retrieval signal of severe acute respiratory syndrome coronavirus to intracellular accumulation of S proteins and incorporation of S protein into virus-like particles. *J Gen Virol* 97:1853–1864. <https://doi.org/10.1099/jgv.0.000494>
46. Mura M, Ruffié C, Billon-Denis E, Combredet C, Tournier JN, Tangy F. 2018. hCD46 receptor is not required for measles vaccine Schwarz strain replication *in vivo*: type-I IFN is the species barrier in mice. *Virology* 524:151–159. <https://doi.org/10.1016/j.virol.2018.08.014>
47. Amanat F, Strohmeier S, Rathnasinghe R, Schotsaert M, Coughlan L, García-Sastre A, Krammer F. 2021. Introduction of two prolines and removal of the polybasic cleavage site lead to higher efficacy of a recombinant spike-based SARS-CoV-2 vaccine in the mouse model. *mBio* 12:e02648-20. <https://doi.org/10.1128/mBio.02648-20>
48. International Coalition of Medicines Regulatory Authorities. 2020. Summary report: Global regulatory workshop on COVID-19 vaccine development. Available from: <https://www.icmra.info/drupal/news/March2020/summary>. Retrieved Mar 2020,23
49. Tseng CT, Sbrana E, Iwata-Yoshikawa N, Newman PC, Garron T, Atmar RL, Peters CJ, Couch RB. 2012. Immunization with SARS coronavirus vaccines leads to pulmonary immunopathology on challenge with the SARS virus. *PLoS One* 7:e35421. <https://doi.org/10.1371/journal.pone.0035421>
50. Anna F, Goyard S, Lalanne AI, Nevo F, Gransagne M, Souque P, Louis D, Gillon V, Turbiez I, Bidard F-C, Gobillon A, Savignoni A, Guillot-Delost M, De Jardin F, Dufour E, Petres S, Richard-Le Goff O, Choucha Z, Helyncq O, Janin YL, Escriou N, Charneau P, Perez F, Rose T, Lantz O. 2021. High seroprevalence but short-lived immune response to SARS-CoV-2 infection in Paris. *Eur J Immunol* 51:180–190. <https://doi.org/10.1002/eji.202049058>
51. Corbett KS, Edwards DK, Leist SR, Abiona OM, Boyoglu-Barnum S, Gillespie RA, Himansu S, Schäfer A, Ziwawo CT, DiPiazza AT, et al. 2020. SARS-CoV-2 mRNA vaccine design enabled by prototype pathogen preparedness. *Nature* 586:567–571. <https://doi.org/10.1038/s41586-020-2622-0>
52. Reuter D, Sparwasser T, Hünig T, Schneider-Schaulies J. 2012. Foxp3<sup>+</sup> regulatory T cells control persistence of viral CNS infection. *PLoS One* 7:e33989. <https://doi.org/10.1371/journal.pone.0033989>
53. Boyd A, Almeida JR, Darrah PA, Sauce D, Seder RA, Appay V, Gorochov G, Larsen M. 2015. Pathogen-specific T cell polyfunctionality is a correlate of T cell efficacy and immune protection. *PLoS One* 10:e0128714. <https://doi.org/10.1371/journal.pone.0128714>
54. Ku M-W, Bourging M, Authié P, Lopez J, Nemirov K, Moncoq F, Noirat A, Vesin B, Nevo F, Blanc C, Souque P, Tabbal H, Simon E, Hardy D, Le Dudal M, Guinet F, Fiette L, Mouquet H, Anna F, Martin A, Escriou N, Majlessi L, Charneau P. 2021. Intranasal vaccination with a lentiviral vector protects against SARS-CoV-2 in preclinical animal models. *Cell Host Microbe* 29:236–249. <https://doi.org/10.1016/j.chom.2020.12.010>
55. Zhuang Z, Lai X, Sun J, Chen Z, Zhang Z, Dai J, Liu D, Li Y, Li F, Wang Y, et al. 2021. Mapping and role of T cell response in SARS-CoV-2-infected mice. *J Exp Med* 218:e20202187. <https://doi.org/10.1084/jem.20202187>
56. Hassan AO, Case JB, Winkler ES, Thackray LB, Kafai NM, Bailey AL, McCune BT, Fox JM, Chen RE, Alsoussi WS, Turner JS, Schmitz AJ, Lei T, Shrihari S, Keeler SP, Fremont DH, Greco S, McCray PB, Perlman S, Holtzman MJ, Ellebedy AH, Diamond MS. 2020. A SARS-CoV-2 infection model in mice demonstrates protection by neutralizing antibodies. *Cell* 182:744–753. <https://doi.org/10.1016/j.cell.2020.06.011>
57. Rathnasinghe R, Strohmeier S, Amanat F, Gillespie VL, Krammer F, García-Sastre A, Coughlan L, Schotsaert M, Uccellini MB. 2020. Comparison of transgenic and adenovirus hACE2 mouse models for SARS-CoV-2 infection. *Emerg Microbes Infect* 9:2433–2445. <https://doi.org/10.1080/22221751.2020.1838955>
58. Hörner C, Schürmann C, Auste A, Ebenig A, Muraleedharan S, Dinnon KH, Scholz T, Herrmann M, Schnierle BS, Baric RS, Mühlebach MD. 2020.

- A highly immunogenic and effective measles virus-based Th1-biased COVID-19 vaccine. *Proc Natl Acad Sci U S A* 117:32657–32666. <https://doi.org/10.1073/pnas.2014468117>
59. Plumet S, Duprex WP, Gerlier D. 2005. Dynamics of viral RNA synthesis during measles virus infection. *J Virol* 79:6900–6908. <https://doi.org/10.1128/JVI.79.11.6900-6908.2005>
  60. Bos R, Rutten L, van der Lubbe JEM, Bakkers MJG, Hardenberg G, Wegmann F, Zuijdgeest D, de Wilde AH, Koornneef A, Verwilligen A, van Manen D, Kwaks T, Vogels R, Dalebout TJ, Myeni SK, Kikkert M, Snijder EJ, Li Z, Barouch DH, Vellinga J, Langedijk JPM, Zahn RC, Custers J, Schuitemaker H. 2020. Ad26 vector-based COVID-19 vaccine encoding a prefusion-stabilized SARS-CoV-2 spike immunogen induces potent humoral and cellular immune responses. *NPJ Vaccines* 5:91. <https://doi.org/10.1038/s41541-020-00243-x>
  61. Qiao H, Pelletier SL, Hoffman L, Hacker J, Armstrong RT, White JM. 1998. Specific single or double proline substitutions in the “spring-loaded” coiled-coil region of the influenza hemagglutinin impair or abolish membrane fusion activity. *J Cell Biol* 141:1335–1347. <https://doi.org/10.1083/jcb.141.6.1335>
  62. Sanders RW, Vesanan M, Schuelke N, Master A, Schiffner L, Kalyanaram R, Paluch M, Berkhout B, Maddon PJ, Olson WC, Lu M, Moore JP. 2002. Stabilization of the soluble, cleaved, trimeric form of the envelope glycoprotein complex of human immunodeficiency virus type 1. *J Virol* 76:8875–8889. <https://doi.org/10.1128/jvi.76.17.8875-8889.2002>
  63. Krarup A, Truan D, Furmanova-Hollenstein P, Bogaert L, Bouchier P, Bisschop IJM, Widjoatmodjo MN, Zahn R, Schuitemaker H, McLellan JS, Langedijk JPM. 2015. A highly stable prefusion RSV F vaccine derived from structural analysis of the fusion mechanism. *Nat Commun* 6:8143. <https://doi.org/10.1038/ncomms9143>
  64. Graham BS. 2016. Vaccines against respiratory syncytial virus: the time has finally come. *Vaccine* 34:3535–3541. <https://doi.org/10.1016/j.vaccine.2016.04.083>
  65. Vogel AB, Kanevsky I, Che Y, Swanson KA, Muik A, Vormehr M, Kranz LM, Walzer KC, Hein S, Güler A, et al. 2021. BNT162b vaccines protect rhesus macaques from SARS-CoV-2. *Nature* 592:283–289. <https://doi.org/10.1038/s41586-021-03275-y>
  66. Liu R, Americo JL, Cotter CA, Earl PL, Erez N, Peng C, Moss B. 2021. One or two injections of MVA-vectored vaccine shields hACE2 transgenic mice from SARS-CoV-2 upper and lower respiratory tract infection. *Proc Natl Acad Sci U S A* 118:e2026785118. <https://doi.org/10.1073/pnas.2026785118>
  67. Capone S, Raggioli A, Gentile M, Battella S, Lahm A, Sommella A, Contino AM, Urbanowicz RA, Scala R, Barra F, et al. 2021. Immunogenicity of a new gorilla adenovirus vaccine candidate for COVID-19. *Mol Ther* 29:2412–2423. <https://doi.org/10.1016/j.ymthe.2021.04.022>
  68. Sanchez-Felipe L, Verduyck T, Sharma S, Ma J, Lemmens V, Van Looveren D, Arkalagud Javarappa MP, Boudewijns R, Malengier-Devliebs B, Liesenborghs L, et al. 2021. A single-dose live-attenuated YF17D-vectored SARS-CoV-2 vaccine candidate. *Nature* 590:320–325. <https://doi.org/10.1038/s41586-020-3035-9>
  69. Mercado NB, Zahn R, Wegmann F, Loos C, Chandrashekar A, Yu J, Liu J, Peter L, McMahan K, Tostanoski LH, et al. 2020. Single-shot Ad26 vaccine protects against SARS-CoV-2 in rhesus macaques. *Nature* 586:583–588. <https://doi.org/10.1038/s41586-020-2607-z>
  70. Lu M, Dravid P, Zhang Y, Trivedi S, Li A, Harder O, Kc M, Chaiwatpongskorn S, Zani A, Kenney A, et al. 2021. A safe and highly efficacious measles virus-based vaccine expressing SARS-CoV-2 stabilized prefusion spike. *Proc Natl Acad Sci U S A* 118:e2026153118. <https://doi.org/10.1073/pnas.2026153118>
  71. Cattin-Ortolá J, Welch LG, Maslen SL, Papa G, James LC, Munro S. 2021. Sequences in the cytoplasmic tail of SARS-CoV-2 spike facilitate expression at the cell surface and syncytia formation. *Nat Commun* 12:5333. <https://doi.org/10.1038/s41467-021-25589-1>
  72. Li S, Kong L, Yu X. 2015. The expanding roles of endoplasmic reticulum stress in virus replication and pathogenesis. *Crit Rev Microbiol* 41:150–164. <https://doi.org/10.3109/1040841X.2013.813899>
  73. Castilow EM, Olson MR, Varga SM. 2007. Understanding respiratory syncytial virus (RSV) vaccine-enhanced disease. *Immunol Res* 39:225–239. <https://doi.org/10.1007/s12026-007-0071-6>
  74. Bolles M, Deming D, Long K, Agnihothram S, Whitmore A, Ferris M, Funkhouser W, Gralinski L, Tatura A, Heise M, Baric RS. 2011. A double-inactivated severe acute respiratory syndrome coronavirus vaccine provides incomplete protection in mice and induces increased eosinophilic proinflammatory pulmonary response upon challenge. *J Virol* 85:12201–12215. <https://doi.org/10.1128/JVI.06048-11>
  75. Honda-Okubo Y, Barnard D, Ong CH, Peng B-H, Tseng C-TK, Petrovsky N. 2015. Severe acute respiratory syndrome-associated coronavirus vaccines formulated with delta inulin adjuvants provide enhanced protection while ameliorating lung eosinophilic immunopathology. *J Virol* 89:2995–3007. <https://doi.org/10.1128/JVI.02980-14>
  76. Fett C, DeDiego ML, Regla-Nava JA, Enjuanes L, Perlman S. 2013. Complete protection against severe acute respiratory syndrome coronavirus-mediated lethal respiratory disease in aged mice by immunization with a mouse-adapted virus lacking E protein. *J Virol* 87:6551–6559. <https://doi.org/10.1128/JVI.00087-13>
  77. DiPiazza AT, Leist SR, Abiona OM, Moliva JI, Werner A, Minai M, Nagata BM, Bock KW, Phung E, Schäfer A, Dinnon KH III, Chang LA, Loomis RJ, Boyoglu-Barnum S, Alvarado GS, Sullivan NJ, Edwards DK, Morabito KM, Mascola JR, Carfi A, Corbett KS, Moore IN, Baric RS, Graham BS, Ruckwardt TJ. 2021. COVID-19 vaccine mRNA-1273 elicits a protective immune profile in mice that is not associated with vaccine-enhanced disease upon SARS-CoV-2 challenge. *Immunity* 54:1869–1882. <https://doi.org/10.1016/j.immuni.2021.06.018>
  78. Iwata-Yoshikawa N, Shiwa N, Sekizuka T, Sano K, Ainai A, Hemmi T, Kataoka M, Kuroda M, Hasegawa H, Suzuki T, Nagata N. 2022. A lethal mouse model for evaluating vaccine-associated enhanced respiratory disease during SARS-CoV-2 infection. *Sci Adv* 8:eab3827. <https://doi.org/10.1126/sciadv.abh3827>
  79. Ebenig A, Muraleedharan S, Kazmierski J, Todt D, Auste A, Anzaghe M, Gömer A, Postmus D, Gogesch P, Niles M, et al. 2022. Vaccine-associated enhanced respiratory pathology in COVID-19 hamsters after T<sub>H</sub>2-biased immunization. *Cell Rep* 40:111214. <https://doi.org/10.1016/j.celrep.2022.111214>
  80. Mateo M, Reynard S, Carnec X, Journeaux A, Baillet N, Schaeffer J, Picard C, Legras-Lachuer C, Allan R, Perthame E, Hillion KH, Pietrosoli N, Dillies MA, Barrot L, Vallve A, Barron S, Fellmann L, Gaillard JC, Armengaud J, Carbonnelle C, Raoul H, Tangy F, Baize S. 2019. Vaccines inducing immunity to Lassa virus glycoprotein and nucleoprotein protect macaques after a single shot. *Sci Transl Med* 11:eaaw3163. <https://doi.org/10.1126/scitranslmed.aaw3163>
  81. Ovsyannikova IG, Dhiman N, Jacobson RM, Vierkant RA, Poland GA. 2003. Frequency of measles virus-specific CD4<sup>+</sup> and CD8<sup>+</sup> T cells in subjects seronegative or highly seropositive for measles vaccine. *Clin Diagn Lab Immunol* 10:411–416. <https://doi.org/10.1128/cdli.10.3.411-416.2003>
  82. van Doremalen N, Lambe T, Spencer A, Belij-Rammerstorfer S, Purushotham JN, Port JR, Avanzato VA, Bushmaker T, Flaxman A, Ulaszewska M, et al. 2020. ChAdOx1 nCoV-19 vaccine prevents SARS-CoV-2 pneumonia in rhesus macaques. *Nature* 586:578–582. <https://doi.org/10.1038/s41586-020-2608-y>
  83. Kis Z, Tak K, Ibrahim D, Papatthanasiou MM, Chachuat B, Shah N, Kontoravdi C. 2022. Pandemic-response adenoviral vector and RNA vaccine manufacturing. *NPJ Vaccines* 7:29. <https://doi.org/10.1038/s41541-022-00447-3>
  84. Gerke C, Frantz PN, Ramsauer K, Tangy F. 2019. Measles-vectored vaccine approaches against viral infections: a focus on chikungunya. *Expert Rev Vaccines* 18:393–403. <https://doi.org/10.1080/14760584.2019.1562908>
  85. Tschismarow R, Van Damme P, Germain C, De Coster I, Mateo M, Reynard S, Journeaux A, Tomberger Y, Withanage K, Haslwanter D, Terler K, Schrauf S, Müllner M, Tauber E, Ramsauer K, Baize S. 2023. Immunogenicity, safety, and tolerability of a recombinant measles-vectored Lassa fever vaccine: a randomised, placebo-controlled, first-in-human trial. *Lancet* 401:1267–1276. [https://doi.org/10.1016/S0140-6736\(23\)00048-X](https://doi.org/10.1016/S0140-6736(23)00048-X)
  86. Pinschewer DD. 2017. Virally vectored vaccine delivery: medical needs, mechanisms, advantages and challenges. *Swiss Med Wkly* 147:w14465. <https://doi.org/10.4414/smw.2017.14465>
  87. Zhu FC, Guan XH, Li YH, Huang JY, Jiang T, Hou LH, Li JX, Yang BF, Wang L, Wang WJ, et al. 2020. Immunogenicity and safety of a recombinant adenovirus type-5-vectored COVID-19 vaccine in healthy adults aged

- 18 years or older: a randomised, double-blind, placebo-controlled, phase 2 trial. *Lancet* 396:479–488. [https://doi.org/10.1016/S0140-6736\(20\)31605-6](https://doi.org/10.1016/S0140-6736(20)31605-6)
88. Brandler S, Ruffié C, Combredet C, Brault J-B, Najburg V, Prevost M-C, Habel A, Tauber E, Desprès P, Tangy F. 2013. A recombinant measles vaccine expressing chikungunya virus-like particles is strongly immunogenic and protects mice from lethal challenge with chikungunya virus. *Vaccine* 31:3718–3725. <https://doi.org/10.1016/j.vaccine.2013.05.086>
  89. Cubitt B, Ly C, de la Torre JC. 2001. Identification and characterization of a new intron in borna disease virus. *J Gen Virol* 82:641–646. <https://doi.org/10.1099/0022-1317-82-3-641>
  90. Lesecure FX, Bouadma L, Nguyen D, Parisey M, Wicky PH, Behillil S, Gaymard A, Bouscambert-Duchamp M, Donati F, Le Hingrat Q, Enouf V, Houhou-Fidouh N, Valette M, Mailles A, Lucet JC, Mentre F, Duval X, Descamps D, Malvy D, Timsit JF, Lina B, van-der-Werf S, Yazdanpanah Y. 2020. Clinical and virological data of the first cases of COVID-19 in Europe: a case series. *Lancet Infect Dis* 20:697–706. [https://doi.org/10.1016/S1473-3099\(20\)30200-0](https://doi.org/10.1016/S1473-3099(20)30200-0)
  91. Boukadida C, Fritz M, Blumen B, Fogeron ML, Penin F, Martin A. 2018. NS2 proteases from hepatitis C virus and related hepaciviruses share composite active sites and previously unrecognized intrinsic proteolytic activities. *PLoS Pathog* 14:e1006863. <https://doi.org/10.1371/journal.ppat.1006863>
  92. Calain P, Roux L. 1993. The rule of six, a basic feature for efficient replication of sendai virus defective interfering RNA. *J Virol* 67:4822–4830. <https://doi.org/10.1128/JVI.67.8.4822-4830.1993>
  93. Schneider H, Kaelin K, Billeter MA. 1997. Recombinant measles viruses defective for RNA editing and V protein synthesis are viable in cultured cells. *Virology* 227:314–322. <https://doi.org/10.1006/viro.1996.8339>
  94. Meier S, Güthe S, Kiefhaber T, Grzesiek S. 2004. Foldon, the natural trimerization domain of T4 fibritin, dissociates into a monomeric a-state form containing a stable  $\beta$ -hairpin: atomic details of trimer dissociation and local  $\beta$ -hairpin stability from residual dipolar couplings. *J Mol Biol* 344:1051–1069. <https://doi.org/10.1016/j.jmb.2004.09.079>
  95. Cokelaer T, Desvillechabrol D, Legendre R, Cardon M. 2017. 'Sequana': a set of Snakemake NGS pipelines. *J Open Source Softw* 2:352. <https://doi.org/10.21105/joss.00352>
  96. Desvillechabrol D, Bouchier C, Kennedy S, Cokelaer T. 2018. Sequana coverage: detection and characterization of genomic variations using running median and mixture models. *Gigascience* 7:giy110. <https://doi.org/10.1093/gigascience/giy110>
  97. Barik S, Das S, Vikalo H. 2018. QSDpR: viral quasispecies reconstruction via correlation clustering. *Genomics* 110:375–381. <https://doi.org/10.1016/j.ygeno.2017.12.007>
  98. Pribjelski A, Antipov D, Meleshko D, Lapidus A, Korobeynikov A. 2020. Using SPAdes *de novo* assembler. *Curr Protoc Bioinform* 70:e102. <https://doi.org/10.1002/cpbi.102>
  99. Schindelin J, Arganda-Carreras I, Frise E, Kaynig V, Longair M, Pietzsch T, Preibisch S, Rueden C, Saalfeld S, Schmid B, Tinevez JY, White DJ, Hartenstein V, Eliceiri K, Tomancak P, Cardona A. 2012. Fiji: an open-source platform for biological-image analysis. *Nat Methods* 9:676–682. <https://doi.org/10.1038/nmeth.2019>
  100. Mrkic B, Pavlovic J, Rüllicke T, Volpe P, Buchholz CJ, Hourcade D, Atkinson JP, Aguzzi A, Cattaneo R. 1998. Measles virus spread and pathogenesis in genetically modified mice. *J Virol* 72:7420–7427. <https://doi.org/10.1128/JVI.72.9.7420-7427.1998>
  101. Hervé P-L, Lorin V, Jouvion G, Da Costa B, Escriou N. 2015. Addition of N-glycosylation sites on the globular head of the H5 hemagglutinin induces the escape of highly pathogenic avian influenza A H5N1 viruses from vaccine-induced immunity. *Virology* 486:134–145. <https://doi.org/10.1016/j.virol.2015.08.033>
  102. Reed LJ, Muench H. 1938. A simple method of estimating fifty per cent endpoints. *Am J Hyg* 27:493–497. <https://doi.org/10.1093/oxfordjournals.aje.a118408>
  103. National Institute for Biological Standards and Control. 2020. Data sheet: research reagent for anti-SARS-CoV-2 Ab. NIBSC code 20/130. Available from: <https://nibsc.org/documents/ifu/20-130.pdf>. Retrieved 29 Feb 2024.
  104. National Institute for Biological Standards and Control. 2020. Data sheet: COVID-19 convalescent plasma panel, human. NIBSC code 20/118. Available from: <https://nibsc.org/documents/ifu/20-118.pdf>. Retrieved 29 Feb 2024.
  105. World Health Organization. 2020. WHO/BS/2020.2403: establishment of the WHO international standard and reference panel for anti-SARS-CoV-2 antibody. Available from: <https://www.who.int/publications/m/item/WHO-BS-2020.2403>. Retrieved 29 Feb 2024.
  106. Corman VM, Landt O, Kaiser M, Molenkamp R, Meijer A, Chu DK, Bleicker T, Brünink S, Schneider J, Schmidt ML, Mulders DG, Haagmans BL, van der Veer B, van den Brink S, Wijsman L, Goderski G, Romette J-L, Ellis J, Zambon M, Peiris M, Goossens H, Reusken C, Koopmans MP, Drosten C. 2020. Detection of 2019 novel coronavirus (2019-nCoV) by real-time RT-PCR. *Euro Surveill* 25:2000045. <https://doi.org/10.2807/1560-7917.ES.2020.25.3.2000045>
  107. Ghibaudo D, Cohen L, Penin F, Martin A. 2004. Characterization of GB virus B polyprotein processing reveals the existence of a novel 13-kDa protein with partial homology to hepatitis C virus p7 protein. *J Biol Chem* 279:24965–24975. <https://doi.org/10.1074/jbc.M401148200>